SYNTHESIS AND CHARACTERIZATION OF PURE AND DOPED STRONTIUM MANGANITE

Dissertation submitted to

Visvesvaraya National Institute of Technology, Nagpur

in partial fulfillment of the requirements for the award of

the degree

Master of Science

in

Physics

by

Rohan Naitame (MS23PHY009)

Under the guidance of

Dr. Oroosa Subohi

Department of Physics

Visvesvaraya National Institute of Technology

Nagpur 440 010 (India)

May 2025

SYNTHESIS AND CHARACTERIZATION OF PURE AND DOPED STRONTIUM MANGANITE

Dissertation submitted to

Visvesvaraya National Institute of Technology, Nagpur

in partial fulfillment of the requirements for the award of

the degree

Master of Science

in

Physics

by

Rohan Naitame (MS23PHY009)

Under the guidance of

Dr. Oroosa Subohi

Department of Physics

Visvesvaraya National Institute of Technology

Nagpur 440 010 (India)

May 2025

© Visvesvaraya National Institute of Technology (VNIT), 2025

VISVESVARAYA NATIONAL INSTITUTE OF TECHNOLOGY, NAGPUR

DEPARTMENT OF PHYSICS

Dissertation approval sheet

Dissertation entitled **"Synthesis and Characterization of Pure and Doped Strontium Manganite"** by **Rohan Naitame** is approved for the degree of Master of Science in Physics.

_____	_____
(*Name*:)	(*Name*:)
Supervisor	**External Examiner**

_____
(*Name*:)
Chairman

Department of Physics

Visvesvaraya National Institute of Technology, Nagpur

Declaration

I, Rohan Naitame, hereby declare that this dissertation titled **"Synthesis and Characterization of Pure and Doped Strontium Manganite"** is carried out by me in the Department of Physics of Visvesvaraya National Institute of Technology, Nagpur. The work is original and has not been submitted earlier whole or in part for the award of any degree/diploma at this or any other Institution / University.

Rohan Naitame

Date:

Certificate

This to certify that the dissertation titled **"Synthesis and Characterization of Pure and Doped Strontium Manganite"** is submitted by **Rohan Naitame** in partial fulfilment of the requirements for the award of the degree of **Master of Science in Physics**, VNIT Nagpur. The work is comprehensive, complete and fit for final evaluation.

Supervisor,
Dr. Oroosa Subohi
Assistant Professor
Dept. of Physics, VNIT, Nagpur

Head, Department of Physics
VNIT, Nagpur
Date:

Visvesvaraya National Institute of Technology, Nagpur

Non-Plagiarism Certificate

Certified that M.Sc. Dissertation titled **"Synthesis and Characterization of Pure and Doped Strontium Manganite"** submitted by **Rohan Naitame** Enrollment No. **MS23PHY009** ID No. **30138** has been checked for plagiarism using TURNITIN software and overlap is found within prescribed limits. A summary of the report is given below;

Rohan Naitame
MS23PHY009

Dr. Oroosa Subohi
Assistant Professor
Dept. of Physics, VNIT, Nagpur

ACKNOWLEDGMENT

This project would not have been possible without the kind support and help of many individuals and organizations. I would not have progressed in my project without their active direction, assistance, cooperation, and encouragement.

Firstly, I would like to thank my project guide **Dr. Oroosa Subohi**, Assistant professor, Department of Physics, VNIT, Nagpur (Maharashtra), for her continuous support and motivation throughout the project work. It has been a great opportunity for me to work under her on academic front. I am also grateful for her constant advice, helping nature, and elderly support which made a significant difference in my life.

I am highly thankful to **Dr. B.R. Sankapal**, Head of Department, Department of Physics, VNIT, Nagpur and all my professors for their invaluable cooperation throughout the session.

I am extremely thankful and pay my special honour to **Mr. Rahul Kumar Sahu (Ph.D. Scholar)** for their endless support and dedicative assistance. In every field either personal or academic, he helped me a lot. His suggested readings and timely guidance made the work easy to understand and manage.

I would wish to thank **Miss Astha Sharma, Miss Archana Wasnik**, **Mr. Amiya Ranjan Sahu (Ph.D. Scholars)** and also my Lab partner **Mr. Tushar Belkhede (M.Sc. student)** for their motive support and sound guidance. They helped me in more ways than one in completing this work.

I would be remiss in not mentioning my parents **Mr. Kiran Kumar** and **Mrs. Rohini** and the whole family, who always encourage me emotionally and financially. They always give me inspiration and hope for doing great in life.

Lastly, I would like to mention my friends and classmates for their cooperation, I am gratefully indebted for their valuable support and understanding.

(Rohan Naitame)

ABSTRACT

In this study, we investigate the synthesis and properties of pure $SrMnO_3$ and the effect of A-site doping with Ba^{2+} and B-site doping with Fe^{3+} and finally at simultaneously doped at both of the sites of $SrMnO_3$ to explore the synergistic effects on its physical properties. A-site doping with alkali-earth elements introduces lattice distortions and modifies the ionic radius mismatch, while B-site substitution with transition metals Fe alters the Mn–O–Mn bond angles and electron bandwidth. Structural analysis confirms hexagonal symmetry (space group *P63/mmc*) for all of the samples. Rietveld refinement reveals lattice distortion defined in terms of

John Teller distortion that enables symmetry breaking, promoting polar behavior of the compound. Magnetization measurements indicate a double hysteresis loop for $Sr_{0.9}Ba_{0.1}Mn_{0.9}Fe_{0.1}O_3$ i.e., enhancement in ferromagnetic ordering due to double exchange interactions facilitated by mixed-valence states. Concurrently, dielectric and polarization studies confirm the emergence or strengthening of dielectric constant of modified $SrMnO_3$, indicating magnetodielectric behavior of the compound. Maximum dielectric constant 523 and minimum loss tangent 0.5 was observed in case of $Sr_{0.9}Ba_{0.1}Mn_{0.9}Fe_{0.1}O_3$ and $Sr_{0.9}Ba_{0.1}MnO_3$ at 100 Hz respectively. These findings suggest that dual-site doping is an effective strategy to engineer multifunctional properties in $SrMnO_3$-based materials for advanced electronic and spintronic applications.

CONTENTS

Declaration....4
Certificate....4
ACKNOWLEDGMENT....7
ABSTRACT....8
LIST OF FIGURES....11
LIST OF TABLES....12
CHAPTER 1....13
INTRODUCTION TO MULTIFERROICS....13
1.1 General Introduction....13
1.2 Multiferroic Materials....14
1.2.1 Ferroelectric Materials....15
1.2.2 Ferromagnetic Materials....16
1.3 Perovskite Structures....17
1.4 Introduction to $SrMnO_{3-\delta}$....18
1.5 Objective of this Work....22
CHAPTER 2....23
SYNTHESIS PROCEDURE....23
2.1 Sol-Gel Combustion Technique....23
2.2 Procedure of Synthesis of Strontium Manganese Oxide ($SrMnO_3$) and....25
its derivatives....25
CHAPTER 3....30
CHARACTERIZATION TECHNIQUES....30
3.1 X-Ray Characterization....30
3.1.1 Powder X-Ray Diffraction....31
3.1.2 Application of X-Ray Diffraction....31
3.2 Raman Spectroscopy....33
3.2.1 Instrumentation of Raman Spectroscopy....34
3.3 Fourier Transform Infrared Spectroscopy....36
3.4 Polarization- Electric Field Hysteresis Loop....38
3.5 Dielectric Analysis....39
3.6 SQUID Analysis....40
CHAPTER 4....42

RESULTS AND DISCUSSION....42
4.1 Introduction....42
4.2 X-Ray Diffraction (XRD) Analysis....42
4.2.1 Rietveld Refinement....45
4.3 Raman Analysis....47
4.4 Fourier Transform Infrared Spectroscopy(FTIR)....48
4.5 Dielectric Analysis....49
4.6 Polarization-Electric Field Loop Analysis....51
4.7 Magnetic Properties....52
CHAPTER 5....55
CONCLUSION AND FUTURE SCOPE....55
5.1 Conclusions....55
5.2 Future Scope....56

LIST OF FIGURES

1.1 Type-I Multiferroic - Lone-Pair mechanism, Geometric ferroelectricity, Charge Ordering.

2.1 Sol-Gel Auto Combustion Process of $SrMnO_3$

2.2 Formation of $SrMnO_3$ and its doped derivatives

2.3 Sol Gel Formation of $Ba_{0.1}Sr_{0.9}MnO_3$(Right) and $SrFe_{0.1}Mn_{0.9}O_3$(Left)

2.4 Pristine $SrMnO_3$ after Auto Combustion

3.1 Schematic diagram of diffraction of X-rays by a crystal (Bragg condition)

3.2 Body of Rigaku smart lab X-ray diffractometer and internal structure of X-ray Diffractometer

3.3 Raman Spectrometer

3.4 Infra-Red spectrometer (Shimadzu-IR Affinity-1)

3.5 The Original Sawyer-Tower circuit for measuring a sample of material

3.6 Schematic of SQUID magnetometer–susceptometer

3.7 Quantum Design MPMS3

4.1 XRD data showing characteristic peaks of (110) with their given JCPDS Card.

4.2 Rietveld Refinement Analysis of $SrMnO_3$ and its Derivatives

4.3 Raman Spectra Analysis of $SrMnO_3$ and its Derivative

4.4 FTIR Spectra analysis

4.5 Dielectric constant and tangent loss with changing frequency of SMO, BSMO, SFMO, BSFMO

4.6 Combined P-E Loop of all samples

4.7 M-H hysteresis curve

4.8 dM/dH curve of SMO, BSMO, SFMO, BSFMO

LIST OF TABLES

4.1 Crystallite Sizes with different methods

4.2 Structural Parameters of $SrMnO_3$ and its Derivatives

4.3 Profile Parameters of $SrMnO_3$ and its Derivatives

4.4 Atomic positions of SMO, BSMO, SFMO, BSFMO with occupancy

4.5 Remanent Polarization and Coercive Field value of SMO and its Doped Derivative

CHAPTER 1

INTRODUCTION TO MULTIFERROICS

1.1 General Introduction

Multiferroic materials are a unique class of substances that exhibit two or more primary ferroic properties simultaneously, such as ferroelectricity, ferromagnetism, and ferroelasticity[1]. It consists of either of spontaneous magnetization, spontaneous polarization, and spontaneous strain. Magnetic order occurs by exchange interactions between magnetic dipoles, originating from unfilled shells of electron orbitals. Electric order is the result of the ordering of local electric dipoles. The coexistence of these properties within a single-phase result in a variety of different physical phenomena and opens up exciting possibilities for novel device applications, particularly in the fields of spintronics, sensors, memory devices, and actuators[2]. For practical purposes, the combination of magnetic order and electric order is mostly used.

The term "multiferroic" itself was first introduced by H. Schmid in 1994, who formally defined materials that exhibit ferroelectric and magnetic ordering simultaneously. In the early studies, materials like $BaTiO_3$ and $PbTiO_3$ were identified as classical ferroelectrics, and transition metal oxides such as Fe_3O_4 (magnetite) were well-known ferromagnets[3]. However, the coexistence of ferroelectricity and ferromagnetism in a single phase was believed to be rare because the mechanisms favouring each ferroic order are generally contradictory at the atomic level.

In the 1970s and 1980s, compounds such as $BiFeO_3$ and $YMnO_3$ were reported to exhibit both ferroelectric and ferromagnetic orders, but their properties were weak and often observed only at low temperatures that limits practical applications. Before the formal definition, several materials exhibiting individual ferroic properties had already been discovered. Ferromagnetism was observed and understood in materials such as iron in the 19th century, while ferroelectricity was first discovered in Rochelle salt (potassium sodium tartrate) by Joseph Valasek in 1920[3]. Recent research has also focused on transition

metal oxides, such as perovskite-type structures, due to their adaptive physical properties and rich phase diagrams.

In summary, multiferroic materials represent a highly interdisciplinary field, combining aspects of condensed matter physics, materials science, and engineering. The exploration of new multiferroic systems, understanding the underlying mechanisms, and enhancing the coupling between different order parameters continue to be major research directions with the promise of enabling next-generation multifunctional devices.

1.2 Multiferroic Materials

Multiferroicity can be shown by materials in a few mechanisms which can be divided into two categories:

Type-I Multiferroic – Type-I multiferroics are good ferroelectrics that show magnetic and electric order independently. It consists of lone pair mechanism, charge ordering, and geometric ferroelectricity.

1) **Lone pair mechanism_–** Certain cations, such as Bi^{3+} and Pb^{2+}, have an active lone pair of electrons (typically $6s^2$ electrons). This feature causes the cation to shift away from the center of the oxygen octahedron, resulting in spontaneous polarization. An example of this phenomenon is $BiFeO_3$. The Bi^{3+} ions possess lone pairs that induce ferroelectricity, while the Fe^{3+} ions contribute to antiferromagnetic ordering[4].
2) **Geometric Ferroelectricity** - In certain compounds, structural distortions—such as the tilting and buckling of polyhedron structure—break inversion symmetry and result in a polar structure, which shows ferroelectricity. In the case of $YMnO_3$, ferroelectricity happens from the geometric tilting and displacement of ions, rather than the presence of electronic lone pairs[5].
3) **Charge Ordering –** Charge Ordering mechanism consists of an alternate arrangement of ions with different valencies in the lattice, which causes ferroelectricity. This nonuniform distribution of valence electrons leads to superstructure or superlattices. For example, in $LuFe_2O_4$, the Fe atom may form a superlattice with an alternating sequence of Fe^{2+} and Fe^{3+} ions[4].

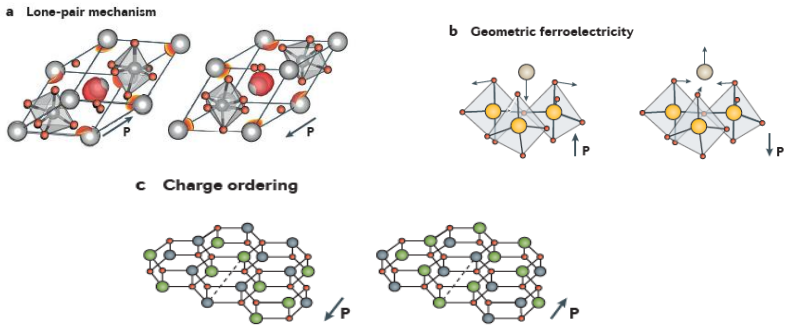

Figure 1.1 - Type-I Multiferroic - (a) Lone-Pair mechanism, (b) Geometric ferroelectricity, (c) Charge Ordering

Type–II Multiferroics - Type II multiferroics are materials in which ferroelectricity is generated by magnetic ordering. In these materials, the magnetic structure directly induces electric polarization, means ferroelectricity arises solely due to the presence of magnetic order.

The mathematical description of multiferroic behavior involves coupling between electric and magnetic parameters, typically represented through tensors and field equations.

This can be described by the relations

$$P_i = \alpha_{ij}H_j + \beta_{ijk}H_jH_k + \ldots \quad (1.1)$$

$$M_j = \alpha_{ji}E_i + \beta_{jik}E_iE_k + \ldots \quad (1.2)$$

It can be also be described by the linear magnetoelectric effect in the expression for the free energy,

$$F_{ME} = -\alpha_{ij}E_iH_j \quad (1.3)$$

The polarization and magnetization are $P = -\partial F/\partial E$ and $M = -\partial F/\partial H$, respectively. From these expressions for free energy, we can derive the first terms in Equations 1.1 and 1.2. This is how the ferroelectric and ferromagnetic ordering are corelated[6].

1.2.1 Ferroelectric Materials

Ferroelectricity is the property of certain materials that exhibit spontaneous electric polarization (Ps). In this phase, these materials can switch polarization between equivalent states when a strong electric field(E) is applied. Their unique characteristic is the ability to show spontaneous polarization, which can be reoriented by external fields. Perovskite ferroelectrics exist in various phases depending on temperature, stress, electric fields, and composition. Above the Curie temperature (T_C), the material becomes non-polar and adopts a cubic structure. Some ferroelectric perovskites have T_C values as high as 450°C. Understanding the behavior of ferroelectric domains under external fields and stress is essential for their applications in energy storage and power generation devices[7]. P-E hysteresis loops illustrate this behavior and characterize a range of classical ferroelectric materials.

1.2.2 Ferromagnetic Materials

The magnetic properties of a materials are closely linked to its crystal structure. The atomic arrangement, lattice symmetry, and the distances between magnetic ions all influence the exchange interactions that causes ferromagnetism[8]. In a crystal, magnetic ions—typically from transition metals such as iron (Fe), cobalt (Co), and nickel (Ni)—are located at specific lattice sites. The overlap of electron orbitals between neighbouring atoms, particularly the partially filled 3d or 4f orbitals, results in an exchange interaction that favors the parallel alignment of spins[2].

The nature of the exchange interaction is influenced by the crystallographic structure of the material[9]. In metallic ferromagnets, the direct exchange mechanism is typically the dominant form of interaction, however, other mechanisms may also be significant depending on the specific crystal structure.

These mechanisms include:

1) **Direct Exchange -** This occurs through the overlap of 3d orbitals between neighbouring atoms, as seen in metals like iron (Fe) and nickel (Ni)[9].
2) **Superexchange -** This is an indirect interaction that occurs through an intervening non-magnetic ion. It is particularly important in oxides such as magnetite[9].

3) **Double Exchange-** This mechanism involves the transfer of electrons between mixed-valence ions, and is commonly observed in manganites[9].

1.3 Perovskite Structures

Perovskite defined by both a structural family and a specific mineral with the composition ABO_3 or ABX_3 . The ideal perovskite features a cubic structure with the space group Pm3m[10]. In this arrangement, the A-atoms are positioned at the corners of the cube, while the B-atoms are located at the center. Oxygen (or halide) atoms occupy the centers of the twelve edges of the cube, creating corner-sharing strings of BO_6 octahedra that extend infinitely in three dimensions. The BO_6 octahedra are perfectly formed with 90° angles and six equal B-O bonds. Each A-atom is surrounded by twelve equidistant oxygen atoms[11]. The perovskite can also be regarded as a cubic close-packed structure in which the oxygen and the A- atoms are stacked in cubic close-packed layers along the cubic [111] direction[11]. Some of the resulting octahedral holes are occupied by B-atoms.

The Goldschmidt tolerance factor (t) provides a simple empirical criterion to predict the structural stability of perovskites:

$$\mathbf{T} = \frac{\mathbf{1}}{\sqrt{\mathbf{2}}} \frac{(\boldsymbol{Rx+Ra})}{(\boldsymbol{Rx+Rb})}$$

are the ionic radii of the A cation, B cation, and X anion, respectively.

1) $\mathbf{t \approx 1}$ - Ideal cubic perovskite.
2) $\mathbf{t < 1}$ - Octahedral tilting occurs to compensate for the size mismatch, leading to lower-symmetry phases.
3) $\mathbf{t > 1}$ - The structure may transform to a hexagonal or other non-perovskite structure.

Few perovskites retain ideal cubic symmetry under ambient conditions. Various structural distortions like octahedral tilting, reduce this symmetry and impact material properties. Octahedral tilting, described by Glazer notation, involves the rotation of BO_6 octahedra around crystallographic axes and is crucial for understanding differences in perovskite

behavior. Another distortion occurs when cations, like Ti^{4+} in ferroelectric perovskites like $BaTiO_3$, are displaced from the center of the oxygen octahedron, creating a permanent electric dipole and inducing spontaneous polarization. In materials like $LaMnO_3$, the presence of transition metal ions with degenerate electronic states can lead to Jahn-Teller distortions, where octahedra are elongated or compressed to lower electronic energy[11].

Distorted perovskite structures can crystallize in different symmetries based on the nature and extent of distortions. Cubic structures occur at high. Tetragonal structures, like $BaTiO_3$, result from polar cation displacements, while orthorhombic structures, such as $CaTiO_3$, arise from octahedral tilting[12]. Rhombohedral structures, seen in $BiFeO_3$, combine polar displacements and octahedral rotations. Each structural variant significantly influences the material's properties. Real perovskites often have point defects and non-stoichiometries that further modify their characteristics. Common oxygen vacancies enhance ionic conductivity and catalytic behavior, while cation vacancies at the A-site or B-site affect electrical and magnetic properties. Anti-site disorder, where A-site and B-site cations are exchanged, also impacts dielectric and magnetic responses[12].

1.4 Introduction to $SrMnO_{3-\delta}$

Strontium manganate ($SrMnO_3$) is a perovskite oxide that has garnered significant interest in materials science due to its interesting dielectric, magnetic, and electronic properties. As a member of the ABO_3 perovskite family, $SrMnO_3$ can exhibit either a cubic or hexagonal crystal structure, depending on the synthesis conditions[13]. The transitions between these structures are influenced by factors such as temperature and doping. Its dielectric properties are closely related to oxygen stoichiometry, Mn oxidation states (Mn^{3+}/Mn^{4+}), and structural distortions, making it suitable for applications in capacitors, sensors, and resistive switching devices[13].

Strontium manganite ($SrMnO_3$) is typically antiferromagnetic at room temperature and below it. Its most stable perovskite structure, manganese ions (Mn^{4+}) interact through superexchange, which involves oxygen atoms[14]. This interaction leads to the antiparallel alignment of neighbouring spins, resulting in no net macroscopic magnetization—a characteristic feature of antiferromagnetism. However, under certain conditions such as

doping, the application of strain, or changes in oxygen content, $SrMnO_3$ can display weak ferromagnetic behaviour.

Moreover, the coupling of $SrMnO_3$ electric and magnetic properties indicates its potential in multiferroic systems[15]. Although progress has been made, challenges persist in optimizing its stability and performance across varying thermal and electrical conditions, highlighting the need for further research on defect engineering and thin-film architectures.

Overall, $SrMnO_3$ serves a model system for understanding structure-property relationships in perovskite oxides, with implications for next-generation electronic and energy storage technologies. There are following available literatures related to SrMnO3.The purpose of this literature survey is to offer a thorough overview of existing research and developments related to the $SrMnO_3$ perovskite structure.

Below given are the literature survey done for this research -

1) P.G.R. Achary et.al. performed synthesis of cerium-doped strontium manganite ($SrMn_{0.94}Ce_{0.06}O_3$) single perovskite using a conventional high-temperature solid-state reaction method. Structural analysis shows that the sample has a hexagonal crystal structure, with an average crystallite size of around 72.2 nm. The addition of the cerium dopant resulted in a lattice strain of about 0.181% in the host matrix. Scanning electron microscopy (SEM) revealed a uniform distribution of grains and distinguishable grain boundaries. The average grain size was found to be around 12.5 μm. Analysis of the dielectric spectra suggests that the grains play a more significant role than the grain boundaries in the conduction mechanism[13].
2) S. Demirel et.al. synthesized $SrMnO_3$ compounds with Mn substituted in $SrCoO_{2.5}$. This substitution prevents the decomposition of the carbonate at 900 °C, thus requiring a temperature of 1200 °C to synthesize the Mn-substituted compounds. Changes in lattice symmetry causes variations in crystal field strength. The temperature-dependent resistivity measurements exhibit hysteretic behavior, which is associated with alterations in oxygen stoichiometry, occurring without any phase transition[16].
3) Corneliu Doroftei et al. conducted a study using a self-combustion method to synthesize the powder, utilizing polyvinyl alcohol as a colloidal medium. After heat treatment for 10 hours at 1000°C, the resulting powder exhibited good

crystalline quality and was free of different phases. It exhibits hexagonal symmetry and is characterized by a fine granulation (about 100 nm), a porous structure. The sample demonstrates the highest catalytic activity for LPG combustion, achieving 92% conversion at 400°C and 95% at 550°C. However, it shows poor performance in the catalytic combustion of toluene and benzene, with conversions of only 50% and 54%, respectively, at 400°C. The preparation procedure of a catalyst influences the concentration of oxygen defects, as well as the structure and activity of its surface-active sites[17].

4) Payel Aich et al. studied the structural and magnetic properties of fluorinated SrMnO3. Their findings indicate that fluorine doping distorts the Mn octahedra, affecting the magnetic properties. A spin or cluster glass-like state appears below 42 K, and a charge-ordering transition occurs around 110 K due to electron doping without structural changes. Additionally, a distorted butterfly loop suggests ferroelectricity after fluorination; however, leakage issues prevented the measurement of the polarization value[18].
5) Gibin George et al. studied porous nanofibers of perovskite SrMnO3, fabricated using a sol-gel assisted electrospinning process followed by calcination. Scanning Electron Microscopy (SEM) revealed a porous morphology, while Transmission Electron Microscopy (TEM) showed nanosized particles. X-ray Diffraction (XRD) analysis confirmed a hexagonal structure of the SrMnO3 nanofibers at 700 °C, which remained stable with up to 20 mol% dopant loading. Doping with 20 mol% Ba significantly increased the specific capacitance from 321.7 F/g to 446.8 F/g at 0.5 A/g, attributed to increased oxygen vacancies from lattice distortions. An asymmetric capacitor device made with these Ba-doped nanofibers achieved a specific capacitance of 423 F/g and an energy density of 37.3 Wh/kg at 400 W/kg. Additionally, the nanofibers maintained 87% of their initial capacitance after 5000 cycles, highlighting their potential in supercapacitor applications[19].
6) S. Hashimoto et al. studied the stabilization of $SrMnO_3$ in the perovskite structure at room temperature by substituting cerium for strontium. The perovskite phase remained stable even after heat treatment at 800°C for 100 hours.

   $Sr_{0.7}Ce_{0.3}MnO_{3-\alpha}$ has a tetragonal crystal structure, with a-axis (3.84 Å) and c-axis (3.86 Å) lengths close to each other, and it showed high conductivity of 290 S/cm

at 1000 °C and 60 S/cm at room temperature. The high conductivity of $Sr_{0.7}Ce_{0.3}MnO_{3-\alpha}$ is attributed to its highly symmetrical structure and a high concentration of charge carriers resulting from the shift of manganese ions from +4 to +3[20].

7) M. Khazaei et al. investigated the formation of the perovskite phase in nano-sized $SrCoO_3$ and $SrMnO_3$, which were prepared using the citrate method. They found that the concentration of citric acid which is used as an emulsifier, significantly affects the formation of the perovskite phase. Specifically, increasing the concentration of this emulsifier leads to a deterioration in perovskite phase formation, resulting in the presence of carbonate and oxide phases instead. Additionally, the study shows that cobalt cations have a greater affinity for forming the perovskite phase compared to manganese cations[21].
8) F. Wang et. al. investigated high-quality epitaxial B-SMO and P-SMO films, noting a phase transition in the M-SMO film. The B-SMO thin film has an orthorhombic structure with ordered oxygen vacancies and exhibits antiferromagnetic properties, while the P-SMO thin film features a tetragonal perovskite structure and shows ferromagnetic properties. The presence of exchange bias suggests that the top perovskite P-SMO phase in the M-SMO film also exhibits ferromagnetism. This behaviour arises from the double exchange coupling between Mn3+ and Mn4+. Controlling oxygen vacancies in perovskite P-SMO can aid future research on multiferroic SrMnO3 thin films, which possess both ferromagnetic and ferroelectric properties. Additionally, the development of the brownmillerite $SrMnO_{2.5}$ film supports the growth of other brownmillerite Mn-based oxide films using traditional deposition methods[14].
9) Aimon Saleem et al. have successfully synthesized the perovskite manganite $SrMnO_3$ using a simple ultrasonic method. The formation of $SrMnO_3$ was confirmed through UV/Vis, FTIR, XRD, and SEM analyses. The morphology assessed by SEM showed the presence of particles with various shapes and sizes. The XRD diffractogram indicated that $SrMnO_3$ has a hexagonal single-phase structure with a crystallite size of 13.67 nm. The perovskite manganite demonstrated the ability to degrade two dyes: malachite green (MG) in 12 minutes and methylene blue (MB) in 4.5 minutes, achieving degradation rates of 80.26%

and 89.35%, respectively. The results of this study confirm the successful formation of $SrMnO_3$ and highlight its potential as an effective photocatalyst[22].

10) Chang Jae Yoon et al. studied the stabilization of a polar state in nonpolar and cubic $SrMnO_3$ (001)-oriented epitaxial thin films through defect induction. Post-deposition annealing was crucial for managing defects by adjusting oxygen vacancies and manganese (Mn) valency. Defects caused variations in the c/a ratio along the growth direction. Investigations using O K-edge and Mn L-edge EELS depth profiling showed a gradual change in oxygen vacancies and Mn valence states across the film, indicating a strain gradient. This interaction of structural parameters contributed to stabilizing polar distortions in the SrMnO3 thin film at room temperature[23].

1.5 Objectives of the present work

This work focuses on the synthesis and characterization of strontium manganese oxide ($SrMnO_3$). The primary objective is to investigate about structure, morphology, electrical, and magnetic properties of $SrMnO_3$.

The study aims to:

- ✓ Synthesize phase-pure $SrMnO_3$ and its doped derivatives using sol-gel auto-combustion methods.
- ✓ Examine the effects of A-site doping (e.g., substituting Sr^{2+} with Ba^{2+} ions) and B-site doping (e.g., partial replacement of Mn with transition metal ions such as Fe) on lattice distortion, ferroelectric properties and magnetic ordering.
- ✓ Explore dual A- and B-site co-doping to synergistically enhance multifunctional coupling particularly targeting room-temperature ferromagnetism and ferroelectricity.

CHAPTER 2

SYNTHESIS PROCEDURE

2.1 Sol-Gel Combustion Technique

Sol-gel self-ignition combustion technique is the combination of sol-gel process and self-ignition combustion technique which involves creating a sol that transforms into a gel through reactions like hydrolysis and condensation and then a self-sustaining combustion reaction where sol-gel mixture reacts exothermically, generating heat and rapidly converting the gel into a solid product[24]. This synthesis is generally used for the formation of bulk oxide.

The Sol-gel process is defined as the making of a inorganic solid using inorganic polymerization reactions induced by water from a precursor solution[25]. Inorganic metal salt or a metal-organic compound such as Alkoxide can be used as the starting compound. As Metal alkoxides react readily with water and can be used for many metals, they are widely used precursors.

The Sol-gel process consists of - (i) The mixing of inorganic salts with water ; (ii) Sol formation from homogeneous solution of Inorganic salts and water ; (iii) aging ; (iv) shaping and v) heat treatment[25]. In the first step, inorganic polymer forms through hydrolysis and condensation reactions. Hydrolysis leads to a sol, a dispersion of colloidal particles in a liquid, and condensation results in a gel, an rigid, and porous inorganic network. This transformation is called the sol-gel transition. Formation of xerogel takes place when gel is dried under ambient conditions[25].

Solution combustion synthesis is simple, and efficient technique having wide number of applications for oxide material. When a fuel and an oxidant in the presence of metal cations ignite a self sustained redox reaction , combustion takes place[26]. The fuel is composed of organics containing carbon and hydrogen that facilitate the liberation of heat by the formation of CO_2 and H_2O during the combustion process.

1) **Role of the fuel –** The Fuel has an important role in deciding the phase formation of the compound. It not only acts as fuel but also as a complexant agent. Complexant agents is used for chelation of metal ions with varying ionic sizes, which helps in prevention of selective precipitation [24]. It is composed by compounds like glycine, urea, hydrazides, citric acid etc., that can react with an oxidant and initializing the combustion reaction[24]. Fuels prevent precipitation of metal ions through chelating agents in fuels and helps in creating strong coordinate bonds preserving the compositional homogeneity[27]. It promotes a gel network after evaporation of solvent that maintain homogeneity of metal cations in their position fixing during the combustion process[28].
2) **Oxygen Balance -** Oxygen balance is the ratio between complexant and salts. According to propellant chemistry, the total valency of metal salts should be balanced by the total valency in the complexant agent[29]. The flame time and its effect on phase formation can be controlled by adjusting the complexant to metal nitrate ratio. An increased excess of complexant in the gels was found to require an external supply of oxygen for the combustion reaction, leading to a decrease in both the reaction rate and temperature[29]. Furthermore, as the complexant concentration increases, more gases are produced, and reaction heat may be transferred to create a system through convection. This will lower the likelihood that particles will come into touch, develop, and fuse together, perhaps creating a powder with a large specific surface area[30]. When the complexant content is insufficient, the system lacks enough reductant to generate adequate heat. As a result, both the reaction rate and temperature decrease, leading to smaller particle sizes and a higher specific surface area.[30]. In comparison with complexant excess systems, less amount of carbon content in the final product could be observed.
3) **Combustion process chemical additive (CPCA) –** The combustion process chemical additives are chemical substances added to a fuel or combustion system to improve the combustion process and enhance efficiency[24]. Ammonia (NH_4OH) is added when citric acid is used as a complexing agent, as it enhances the chelation of metal cations with citrate. This can help regulate the oxygen balance and promote the formation of porous three-dimensional (3D) network structures in nitrate–citrate xerogels[27].

4) **Influence of atmosphere –** The atmosphere plays an important role in controlling the combustion process. *Yu et al.* noticed that a faster reaction process occurs when was flowing air in comparison to a nitrogen environment[31]. The formation of NO^{3-} ions, which function as oxidants, and the addition of more nitrogen to the gel leads to this phenomena. Nitrogen may, however, occasionally limit the oxidation-reduction reaction. Additionally, air has a lower temperature than nitrogen for the synthesis of spinel ferrite following the combustion event[32].
5) **Heating Mechanisms -** Combustion reactions can be initiated using various heating sources, including a muffle furnace, hotplate, microwave, or laser annealing. Among these, the muffle furnace is the most commonly used, as it provides uniform heating to the precursor solution, triggering an intense combustion reaction[24].

2.2 Procedure of Synthesis of Strontium Manganese Oxide ($SrMnO_3$) and its derivatives

The sol-gel auto-combustion technique preferred over other synthesis methods for its simplicity and efficiency, allowing for the production of high-purity, homogeneous materials with controlled properties. It combines the benefits of sol-gel processing, such precise stoichiometric control and uniform mixing, with a self-sustaining combustion reaction, minimizing the need for external heating and reducing processing time. This technique allows for precise doping tailoring of material properties by adjusting precursor composition and combustion parameters. Its cost-effectiveness, scalability, and ability to produce complex oxides[24]

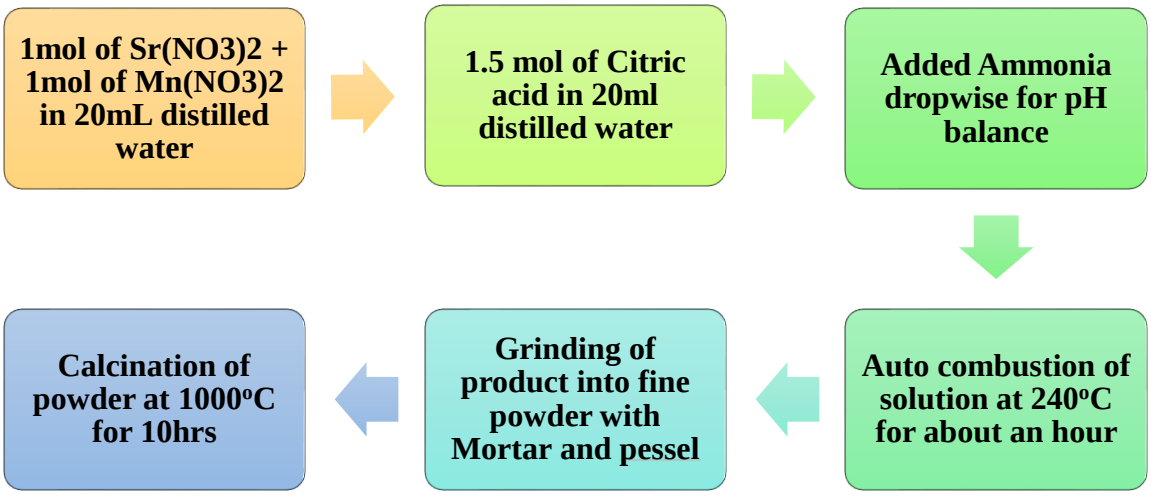
1mol of Sr(NO3)2 + 1mol of Mn(NO3)2 in 20mL distilled water
1.5 mol of Citric acid in 20ml distilled water
Added Ammonia dropwise for pH balance
Auto combustion of solution at 240°C for about an hour
Grinding of product into fine powder with Mortar and pessel
Calcination of powder at 1000°C for 10hrs

Figure 2.1 – Sol-Gel Auto Combustion Process of $SrMnO_3$

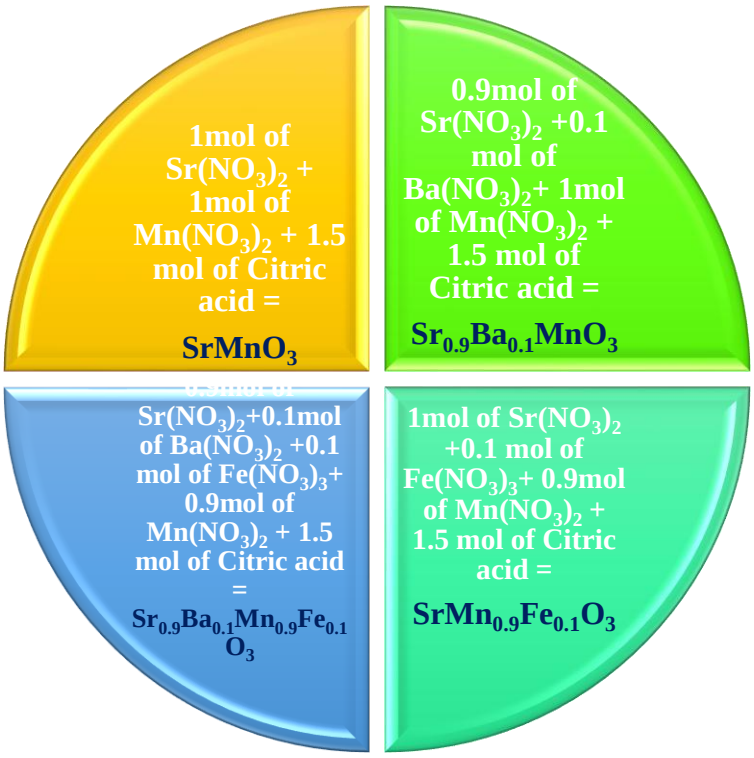
1mol of $Sr(NO_3)_2$ + 1mol of $Mn(NO_3)_2$ + 1.5 mol of Citric acid = $SrMnO_3$
0.9mol of $Sr(NO_3)_2$ +0.1 mol of $Ba(NO_3)_2$+ 1mol of $Mn(NO_3)_2$ + 1.5 mol of Citric acid = $Sr_{0.9}Ba_{0.1}MnO_3$
$Sr(NO_3)_2$+0.1mol of $Ba(NO_3)_2$ +0.1 mol of $Fe(NO_3)_3$+ 0.9mol of $Mn(NO_3)_2$ + 1.5 mol of Citric acid = $Sr_{0.9}Ba_{0.1}Mn_{0.9}Fe_{0.1}O_3$
1mol of $Sr(NO_3)_2$ +0.1 mol of $Fe(NO_3)_3$+ 0.9mol of $Mn(NO_3)_2$ + 1.5 mol of Citric acid = $SrMn_{0.9}Fe_{0.1}O_3$

Figure 2.2 – Formation of $SrMnO_3$ and its doped derivatives

For the synthesis of SrMnO3, Strontium Nitrate [$Sr(NO_3)_2$], Manganese Nitrate [$Mn(NO_3)_2$], Citric acid[$C_6H_7O_8$] were used as precursor. In a beaker, 2.11g of $Sr(NO_3)_2$ and 2.51g of $Mn(NO_3)_2$ is mixed with 20ml of distilled water with the help of a magnetic stirrer. In another beaker, 1.5 mol i.e 2.88g of citric acid is mixed with 20ml of distilled water. After complete dissolving into a solution, both solutions are mixed into a single beaker and and is stirred for homegenisation. For pH balance of the solution, ammonia (NH_3) is added dropwise so that solution become nearly neutral as it was highly acidic due to the presence of nitrate. After stirring for one hour, it changes into a slurry.

Then, this solution is kept in hot air oven which is set at 240^oC for 1-2 hours, auto combustion occurs and $SrMnO_3$ is formed Keeping it overnight for cooling to its room temperature, then grinding done with the help of mortar and pestle until its turn into fine powder. Powder is transferred into alumina crucible and kept in furnace for calcination at 1000^oC for 10hrs and the desired product is obtained.

For making its derivative, we doped first the A-site by adding 0.1 mol of $Ba(NO_3)_2$ ($Sr_{0.9}Ba_{0.1}MnO_3$), then doped the B-site by adding 0.1 mol of $Fe(NO_3)_3$ ($SrMn_{0.9}Fe_{0.1}O_3$) and then we doped both A and B-site simultaneously by adding $Ba(NO_3)_2$ and $Fe(NO_3)_3$ in same molar quantity in their respective sites($Sr_{0.9}Ba_{0.1}Mn_{0.9}Fe_{0.1}O_3$).The reported value of citric acid for Ba- doped SrMnO3 is 1.6 mol, Fe-doped is 1.1 mol and both sites doped is 1.13 mol but we used 1.5 mol of Citric acid for all the procedure of synthesis of doped samples.

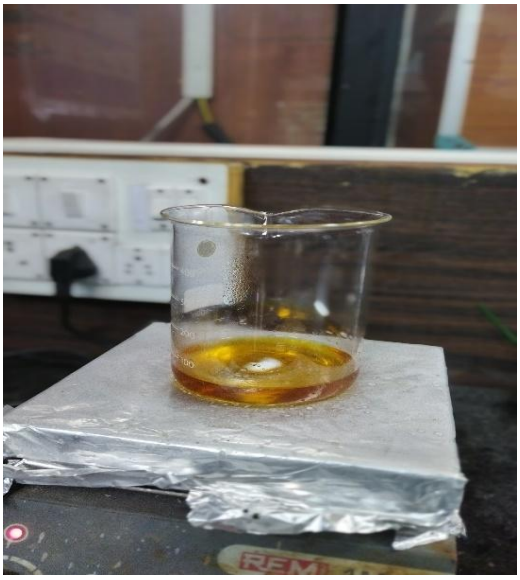

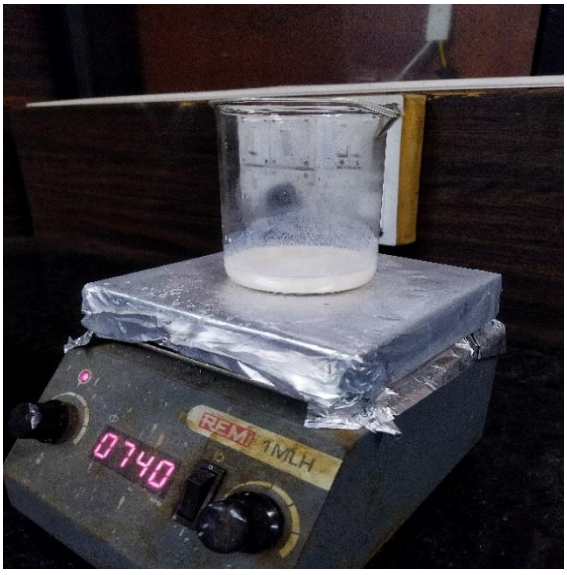

Figure 2.3 – Sol Gel Formation of $Ba_{0.1}Sr_{0.9}MnO_3$(Right) and $SrFe_{0.1}Mn_{0.9}O_3$(Left)

After the formation of powdered samples which are calcined, the process of pellet formation takes where the powdered samples are pressed into small pellet to study the magnetic and electric properties of the materials. Pellets is about 0.5mm thickness for pristine sample and 1mm thickness for doped samples with radius of 5mm was prepared. For pellet formation, powdered sample is ground for 1 hr to convert it into very fine particles. Then Polyvinyl Alcohol(PVA) is added in the fine sample to provide binding effect to the material that helps in making the pellet. Hydraulic press is used for pellet making in which pellet formed by hydraulic pressure put on pellet. In this case, 9 kg/m^3 of pressure is applied for 15-20 min for pellet formation. Then, Pellet is sintered in muffle furnance in following steps – 1) Setting segment 1 from 77^oC to 500^oC for 3hr 32min at the ramp rate of 2^o/min; 2) Setting soak time at 500^oC for 13hr in which the PVA is evaporated; 3) Temperature change from 500^oC to 1000^oC for 4hr 10min in segment 2; 4) Setting soak time at 1000^oC for 6hr to get the solid pellet for characterization of material.

Figure 2.4 – Pristine $SrMnO_3$ after Auto Combustion

For this research, the samples are name with code:-

$SrMnO_3$–SMO

$Ba_{0.1}Sr_{0.9}MnO_3$ – BSMO

$SrFe_{0.1}Mn_{0.9}O_3$ – SFMO

$Ba_{0.1}Sr_{0.9}Fe_{0.1}Mn_{0.9}O_3$ - BSFMO

CHAPTER 3

CHARACTERIZATION TECHNIQUES

3.1 X-Ray Characterization

X-ray diffraction is the analytical technique used for the identification of the material by using an X-ray source and the phenomenon of diffraction. It happens when X-ray falls onto atoms and gets scattered through it. Due to distinct and regular arrangement of atoms, it gives 'fingerprint' patterns[33].

This technique is useful for the identification of the various phases in a material. It can be helpful in finding the crystal structure of material including its lattice parameters, crystallite size and its orientation.

The primary goal of X-ray diffraction in crystals is to determine the specific conditions under which the scattered X-rays from atoms are in phase with the incident X-rays, allowing them to constructively interfere and generate a detectable diffraction beam.

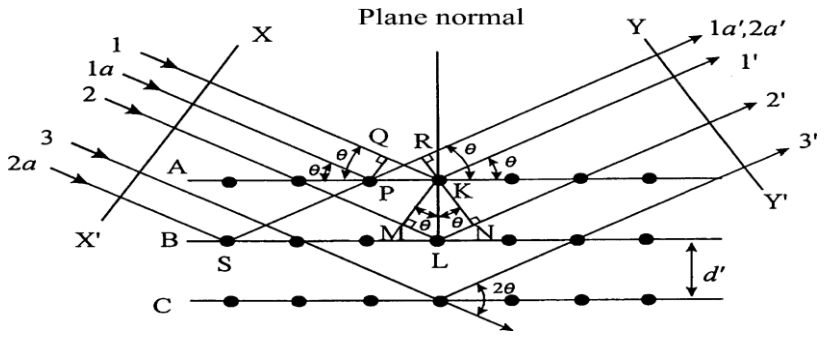

Figure 3.1 - Schematic diagram of diffraction of X-rays by a crystal (Bragg condition)

When a monochromatic X-ray beam passes through a crystalline material, the waves are scattered by the electron clouds surrounding the atoms. Constructive interference occurs when the path difference between reflected waves satisfies Bragg's Law:

$$n\lambda=2d\sin\theta_n$$

where n is the order of reflection, λ is the wavelength of the incident X-rays, d is the spacing between crystallographic planes, and θ is the angle of incidence (Bragg angle)[33]. By measuring the angles and intensities of these diffracted beams, it is possible to infer the structure of the crystal.

3.1.1 Powder X-Ray Diffraction

Powder X-ray diffraction (PXRD) is employed to analyze polycrystalline materials in the form of powders, pellets, and thick films. In this technique, the sample is rotated within the path of a collimated X-ray beam at a fixed incidence angle (θ), while a detector positioned at an angle of 2θ collects the diffracted X-rays[34]. A goniometer is used to control the sample's rotation and maintain the correct incidence angle[34].

In this setup, the X-ray source, sample, and detector are aligned along the circumference of a focusing circle, improving beam focus. The sample is at the center, while the source and detector sit on the edge. The scattering vector (Q) and surface normal (S) are vertically aligned, and a graphite curved crystal monochromator in front of the detector has a divergence of about 0.1 degrees[34]

3.1.2 Application of X-Ray Diffraction

3.1.2.1 Phase identification

X-ray diffraction (XRD) is a quick method to gather information about the phase formation in a sample and its crystalline quality, whether as a single crystal or polycrystal with preferred or non-preferred orientation. The indexing of XRD peaks is typically accomplished using three main techniques:

(a) Comparison, where the measured pattern is matched with standard International Crystallographic Data (ICDD) files; (b) analytical; (c) graphical[34]. By comparing the positions and intensities of three or more intense peaks from the XRD pattern with ICDD files, researchers can identify the crystalline phase of the sample.

3.1.2.2 Structure Determination

Crystals with precise periodicity produce sharp X-ray diffraction (XRD) peaks. A slow scan speed is preferred for clear XRD profiles. By indexing the XRD pattern from cubic to monoclinic, you can determine the sample's structure. Once a cubic structure is identified, various forms (simple cubic, body-centered cubic, or face-centered cubic) can be estimated using (hkl) peaks and ($h^2 + k^2 + l^2$) values[34]. Ratios of 1, 2, 3, 4, 5, 6, 8, or 9 indicate a simple cubic structure, while even ratios suggest a body-centered cubic (BCC) structure. Ratios of 3, 4, 8, or 11 correspond to face-centered cubic (FCC)[34]. Rietveld refinement analysis can also be applied to known polycrystalline or multiphase samples to identify the structure and determine lattice parameters.

3.1.2.3 Crystallite size and strain determination

X-ray diffraction (XRD) is commonly employed to determine the crystallite size and strain in materials. However, when estimating crystallite size using the full width at half maximum (FWHM) of the XRD peak, the results can be overestimated. This occurs because larger crystallites or grains contribute more intensely to the peak, while smaller ones tend to merge into the base, reducing their visibility. To address this, Scherrer proposed an equation which is known as the Scherrer equation—which calculates crystallite size based on the integral breadth of the diffraction profile.

$$\mathbf{D} = \frac{\mathbf{k\lambda}}{\boldsymbol{\beta}\mathbf{cos\theta}}$$

where $\boldsymbol{\lambda}$ represents the X-ray wavelength, while **D** denotes the average particle size. The parameter $\boldsymbol{\beta}$ ($\Delta 2\theta$) refers to the full width at half maximum (FWHM) of the diffraction peak observed at the angle 2θ. The constant **k**, known as the Scherrer constant, is a dimensionless shape factor. Although its value is typically around 0.9, it was later recognized that the exact value of **k** depends on the shape and geometry of the crystallites[33]

In 1953, Williamson and Hall introduced a method for determining particle size and strain in nanomaterials by analyzing the broadening of X-ray diffraction (XRD) peaks, now known as the Williamson-Hall (WH) plot method[34]. This technique effectively distinguishes the contributions of particle size and strain to XRD peak broadening, allowing for calculations of microstrain and particle size in a sample.

$$\beta\cos\theta = k\lambda/D + 4\varepsilon\sin\theta$$

In the given equation, λ, β, and k are defined, and ε denotes the sample's microstrain. By plotting βcosθ against sinθ for a specific diffraction pattern of polycrystalline samples, a straight line is obtained. The slope and intercept of this line provide values for microstrain and average particle size[34].

Figure 3.2 - Left –Body of Rigaku smart lab x-ray diffractometer, Right – Internal arrangement of XRD machine [Department of Physics, VNIT Nagpur, Maharashtra]

3.2 Raman Spectroscopy

Raman spectroscopy is a spectroscopic technique typically used to determine vibrational, rotational and other low-frequency modes of systems. This spectroscopy is commonly used to provide a structural fingerprint by which molecules can be identified. It is based on the principle of Raman Scattering. When monochromatic radiation of frequency ν_0 is directed at a sample, part of the radiation is scattered. Along with radiation at the same

frequency as the incident light (Rayleigh scattering), scattered radiation with different frequencies—known as Raman radiation—is also observed[35].

Inelastic scattering involves the interaction of a photon with a molecule. When a photon of energy $h\nu_0$ interacts with a molecule, it may be virtually absorbed, leading to the creation of a new photon with energy $h(\nu_0 - \nu_M)$ as the molecule transitions to an excited vibrational state. If the molecule is already in an excited state, the photon can be annihilated, resulting in a new photon of energy $h(\nu_0 + \nu_M)$, while the molecule moves to a lower energy state[35]

The Classical theory of Raman effect gives us the concept of polarizability of molecule where a molecule get distorted when placed in a static electric field. Due to separation of charges of molecule , induced electric dipole are set up in the field and molecule are said to be polarized[36].

$$\mu = E\alpha$$

μ= size of induced dipole

α= polarizability of molecule

E= Magnitude of applied field

The electric field of radiation oscillates at a frequency ν_0, inducing a corresponding oscillation in the dipole moment of the molecule[36]. The polarizability α of the molecule can vary slightly over time at a slower vibrational frequency ν_M, leading to amplitude modulation of the dipole moment.

This modulation can be broken down into three frequency components: ν_0, $\nu_0+\nu_M$, and $\nu_0-\nu_M$[36]. The resulting dipole moment oscillations can emit scattered radiation at these frequencies, known as Rayleigh, Raman anti-Stokes, and Raman Stokes frequencies. If there is no variation in polarizability due to molecular vibration, amplitude modulation, and consequently Raman Stokes or anti-Stokes emission, will not occur[36]

3.2.1 Instrumentation of Raman Spectroscopy

The mercury arc lamp was used as a light source in Raman spectrophotometers until the 1960s[37]. Now, various lasers like Argon ion (488 and 514.5 nm), Krypton ion (530.9 and 647.1 nm), He-Ne (632.8 nm), Near Infrared diode lasers (785 and 830 nm), and

Nd:YAG (1064 nm) are commonly employed[37]. Short-wavelength sources, such as Argon and Krypton ion lasers, often induce significant fluorescence and photodecomposition in samples. Conversely, long-wavelength sources like diode and Nd:YAG lasers can operate at higher power levels while minimizing the risk of fluorescence and photodecomposition[37].

Band-pass filters are used to isolate a specific laser beam. In dispersive instruments, the most common setup includes a notch filter combined with a high-quality grating monochromator. To effectively separate the relatively weak Raman signals from the intense Rayleigh scattered radiation, instruments may employ double or triple grating monochromators, super notch filters, rejection filters, holographic notch or edge filters, and other types of holographic filters[37].

Early models of dispersive Raman spectrophotometers used thermoelectrically cooled photomultiplier tubes and photodiode array detectors. However, with advances in instrumentation and technology, these older detectors have been replaced by more sensitive charge transfer devices (CTDs), such as charge-coupled devices (CCDs) and charge-injection devices (CIDs)[37]. These devices function as detectors and are commonly used in array formats. In charge transfer device (CTD) arrays, each photosite converts incoming optical signals into electrical charges, which are then accumulated and transferred to readout components. Multichannel CCD detectors are typically employed with laser wavelengths below 1 μm, whereas single-element low band-gap semiconductors like Germanium (Ge) or Indium–Gallium–Arsenic (InGaAs) are used for wavelengths above 1 μm[37].

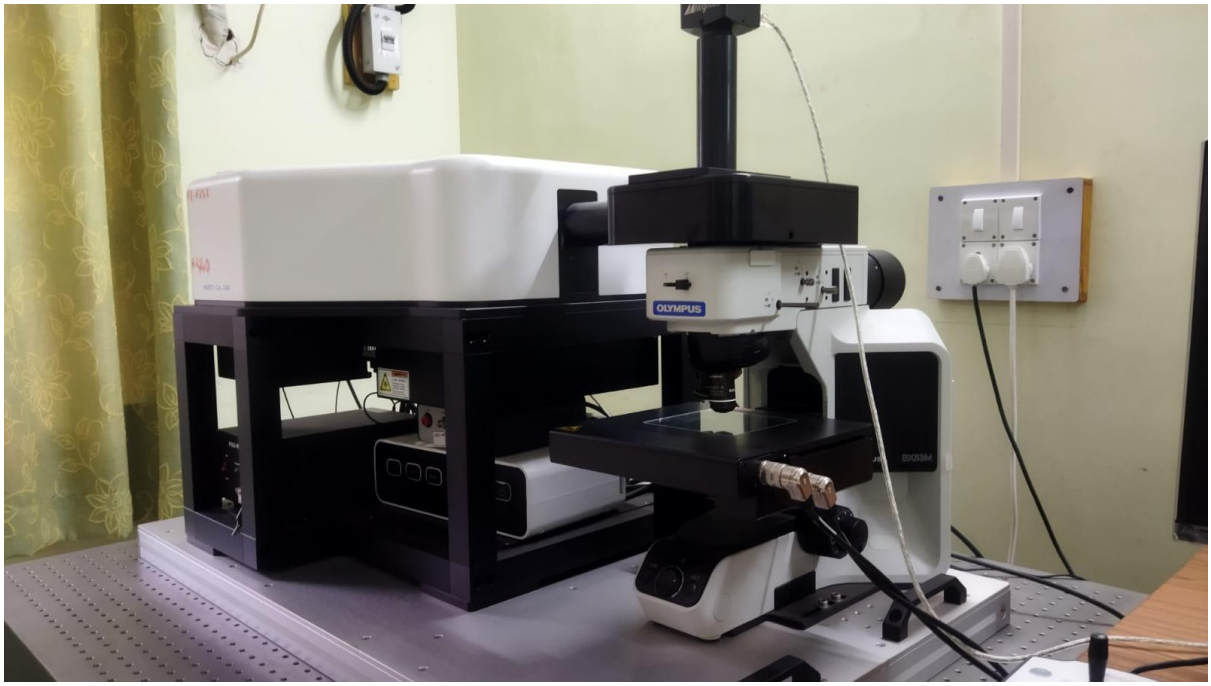

Figure 3.3 – Raman Spectrometer [Department of Physics, VNIT Nagpur, Maharashtra]

3.3 Fourier Transform Infrared Spectroscopy

Fourier transform infrared (FTIR) spectroscopy has a wide range of applications, spanning from the analysis of small molecules or molecular complexes to the study of materials.

A beamsplitter in this device divides an incoming collimated beam of light into two directions. One of these paths has a fixed length, while the other can be adjusted by moving a mirror[38]. The beamsplitter then recombines the two beams so that, on average, half of the light travels through an absorbing sample before returning to the source, while the other half goes to a detector. When the two beams recombine at the beamsplitter, the movement of the mirror creates a path difference, leading to a phase difference between them[38]. This results in interference between the beams.

The signal recorded at the detector, known as the interferogram, exhibits a sinusoidal pattern when using a monochromatic source and a mirror moving at a constant speed. For a polychromatic source, the interferogram is the combined output of the sinusoidal signals from each distinct wavelength emitted by the source[38]. These sinusoidal signals from each wavelength are in phase only when the stationary and moving mirrors are equally spaced. At this point, the amplitude of the interferogram is exceptionally large[38]A very slight phase shift exists between all the waves, which can be confirmed by initially recording a single-beam background spectrum. Once this is done, the sample is placed in the beam path, and its single-beam spectrum is subsequently measured. The transmittance of the sample is determined by calculating the ratio of these two spectra. Additionally, the absorbance spectrum is often obtained by computing the negative logarithm of the transmittance spectrum[39].

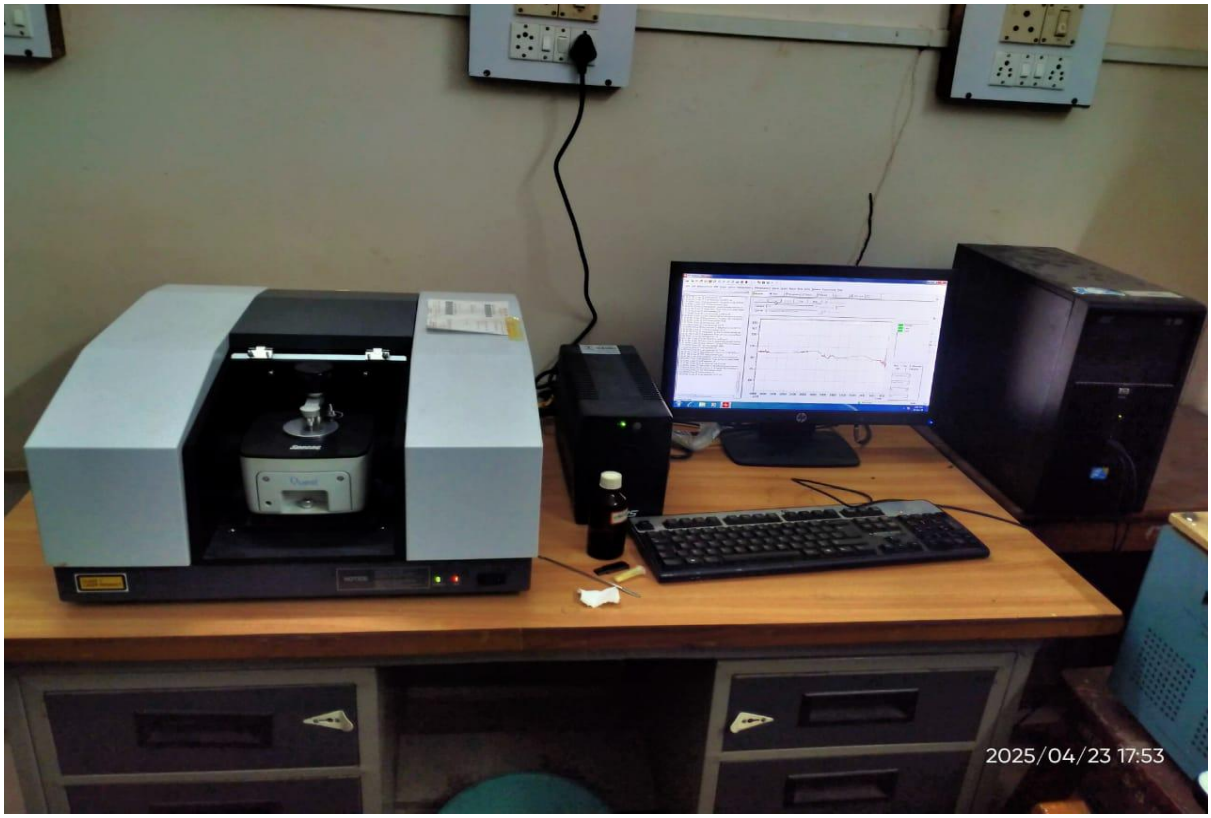

Figure 3.4 - Infra-Red spectrometer (Shimadzu-IR Affinity-1) [Department of Chemistry, VNIT Nagpur, Maharashtra]

3.4 Polarization- Electric Field Hysteresis Loop

Polarization-Electric field loop is analysed with the help of the Sawyer Tower Circuit. The plotting of P-E curve standard parameters from this circuit allows one to anticipate the polarization value and order area of materials, in addition to interpreting electrical characteristics[40].The basic standard configuration of the probe is designed for materials testing, utilizing a two-probe mechanism to apply an electric field to the sample and subsequently measure the sample's voltage response (i.e., its capacitance-voltage characteristics)[40].

The configuration of the thin substrate and probe is crucial for obtaining efficient and precise measurements from the material. In this research, a Si-substrate with a thickness of 900 nm was chosen[40]. The polarization and electrical field injection can be plotted through the use of a probe. An optimized probe was selected for implementing the Sawyer-Tower circuit, which is used for the characterization of ferroelectric materials.

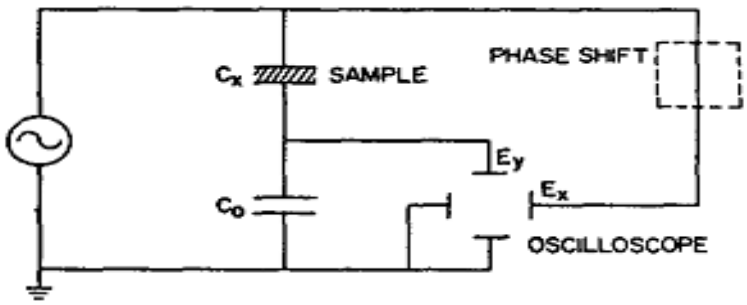

Figure 3.5- The Original Sawyer-Tower circuit for measuring a sample of material

One popular method for determining the polarization-electric field (P-E) hysteresis loops of ferroelectric materials is the Sawyer-Tower circuit. This technique works by applying an alternating voltage across a series combination of a reference capacitor (C_{REF}), which has a known capacitance, and a ferroelectric capacitor (C_{FE})[40]. Since the capacitors are connected in series, they experience the same charge displacement, and the voltage across the reference capacitor is proportional to the charge stored in the ferroelectric material. This allows for the indirect measurement of polarization[40].

A change in the electric field across the ferroelectric material results in a shift in its polarization when an alternating voltage is applied. The voltage across the reference

capacitor changes as a result of the ferroelectric capacitor's charge fluctuating appropriately[40]. The relationship $P=Q/A$, where Q is the charge and A is the area of the capacitor electrodes, can be used to calculate the polarization P of the ferroelectric material by measuring this voltage. Plotting P against E on an oscilloscope yields the ferroelectric material's distinctive hysteresis loop.

The hysteresis loop reveals key ferroelectric properties, such as the coercive field (Ec), the strength needed to reverse polarization, and remanent polarization (Pr), which indicates the polarization remaining after the electric field is removed. The Sawyer-Tower circuit is essential for assessing these materials, as it allows researchers to study their switching behavior and dielectric properties in alternating electric fields, crucial for applications in memory devices, sensors, and actuators[40]

3.5 Dielectric Analysis

In high-frequency circuits, understanding the dielectric properties of materials—such as dielectric constant, tangent loss, impedance, and capacitance—is essential. Dielectric measurements are important for applications in energy storage and solid-state electronics.

Impedance spectroscopy is an analytical technique used to investigate the dielectric properties of materials across a range of frequencies and temperatures. The dielectric constant indicates how easily a material can be polarized and how much polar molecules resist movement when exposed to an electric field[41]. Mathematically,

$$\varepsilon_r = 1+P/\varepsilon_o E$$

where, ε_r is dielectric constant

P is induced dipole moment per unit Volume

ε_o is permittivity of free space

The dielectric constant of a dielectric material is affected by changes in temperature and the frequency of the applied electric field. Generally, as temperature and frequency increase, the dielectric constant tends to decrease[41]. The dielectric loss factor, also known as the loss tangent (tan δ), measures the amount of energy dissipated or lost in a dielectric material when subjected to an alternating electric field. This loss factor is

calculated by dividing the energy loss (loss factor) by the dielectric constant, which indicates the material's ability to store energy[41].

$$\tan\delta = \varepsilon``/\varepsilon`$$

where , $\varepsilon``$ = Loss factor

$\varepsilon`$ = Dielectric constant

3.6 SQUID Analysis

A SQUID (superconducting quantum interference device) is made up of a superconducting loop that contains a weak link, allowing current to flow through it via quantum mechanical tunneling. The SQUID is highly sensitive to minor changes in magnetic fields. This sensitivity allows it to detect variations in magnetic flux caused by the proximity of a paramagnetic sample[42]. The resulting signal is amplified, making SQUID the most accurate technique available for measuring magnetic susceptibility[42]

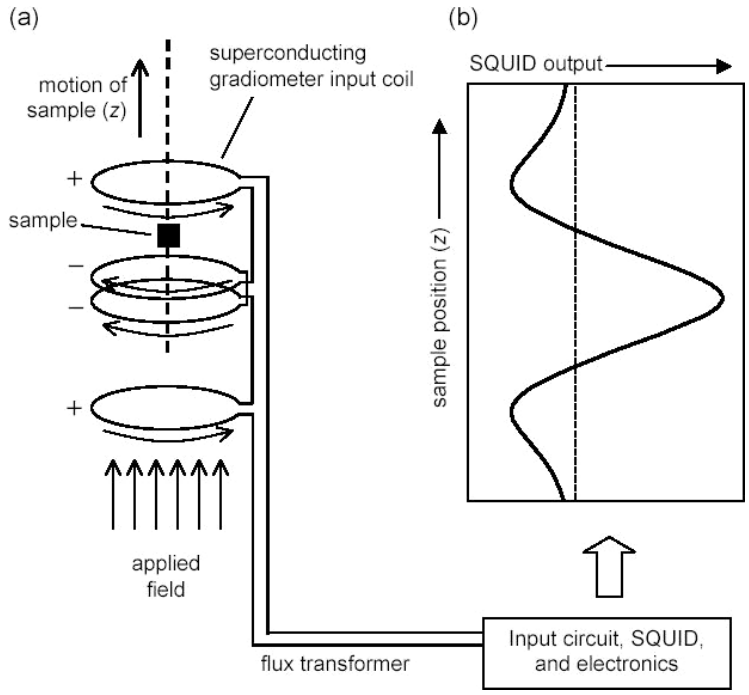

Figure 3.6 – (a) Schematic of SQUID magnetometer–susceptometer, (b) Calibrated output from SQUID electronics, recorded as a function of position

For measurement, a sample—typically only a few millimeters in size—is mounted onto a sample rod. This rod is then passed through the center of a first- or second-order superconducting gradiometer[42]. This gradiometer acts as a closed flux transformer, which is connected to a SQUID (Superconducting Quantum Interference Device). The signal from the SQUID is usually recorded based on the position of the sample[42]. By analyzing the shape and magnitude of the resulting response curve with a computer, it is possible to determine the corresponding magnetic moment of the sample. A magnetic field is applied to the sample by positioning the detection coils inside the bore of a superconducting magnet. Temperature control is maintained by placing the sample and sample rod inside a sealed variable temperature insert, which is thermally isolated from the 4.2-K gradiometer and the magnet via an annular vacuum space[43]

Figure 3.7 - Quantum Design MPMS3 [Institute Instrumentation Centre, IIT Roorkee, Uttarakhand]

CHAPTER 4

RESULTS AND DISCUSSION

4.1 Introduction

Pure and doped $SrMnO_3$ powder samples were synthesized using the sol-gel auto-combustion technique. The gel was dried in a hot air oven at 240 °C until autocombustion took place followed by calcination at 1000 °C for 10 hours to obtain the pure crystalline powder. The resulting powder was then pressed into pellets under a pressure of 9 kg/cm^2 for 15–20 minutes using a hydraulic press. The sintering process was conducted in two thermal segments. In the first segment, the temperature was increased from room temperature to 500 °C over a period of 3 hours and 32 minutes, followed by a soaking period at 500 °C for 13 hours. In the second segment, the temperature was ramped from 500 °C to 1000 °C over 4 hours and 10 minutes, followed by a soaking stage at 1000 °C for 6 hours, during which the final sintering occurred.

In this chapter, we present a detailed analysis of the electrical, magnetic, and dielectric properties of $SrMnO_3$ and its doped derivatives.

4.2 X-Ray Diffraction (XRD) Analysis

X-ray diffraction (XRD) data obtained for the synthesized $SrMnO_3$ and its doped derivatives are presented below. The diffraction patterns of all samples closely match the standard JCPDS card No. 24-1213, with the exception of the (104) peak, which aligns with JCPDS No. 24-1221. This deviation suggests the successful incorporation of barium and iron ions into the $SrMnO_3$ lattice structure.

Multiple diffraction peaks with secondary phases observed after calcination of the powder at 900^oC as per the earlier results[17], confirming the formation of crystalline but impure phases. The XRD patterns imply that a thermal treatment above 900 °C is required to achieve sufficient crystallinity. After heat treatment at 1000 °C for 10 hours, the appearance of sharp, well-defined peaks in the diffraction pattern indicates the formation

of a high-quality crystalline structure, free from secondary or impurity phases. Based on the standard JCPDS No. 24-1213, the material crystallizes in a hexagonal structure with space group P63/mmc. The calculated lattice parameters (a = 5.454 Å; c = 9.090 Å) are in good agreement with values previously reported in the literature[17].Figure 4.1 presents due to incorporation of Barium in A-site, it leads to lattice expansion as ionic radii of Ba is greater than Sr. This leads peaks shift toward lower value of 2θ. When Fe ions are doped in $SrMnO_3$, we observed that the peaks become broader and their intensity drastically decreases. This happens because as Fe is doped, it introduces the structural deformation in the lattice which leads to broader peak and low intensity. When we doped both A- and B-sites together, we get combined effect of lattice expansion and structural deformation which leads to shifted and low intensity, broader peak of $Ba_{0.1}Sr_{0.9}Fe_{0.1}Mn_{0.9}O_3$.

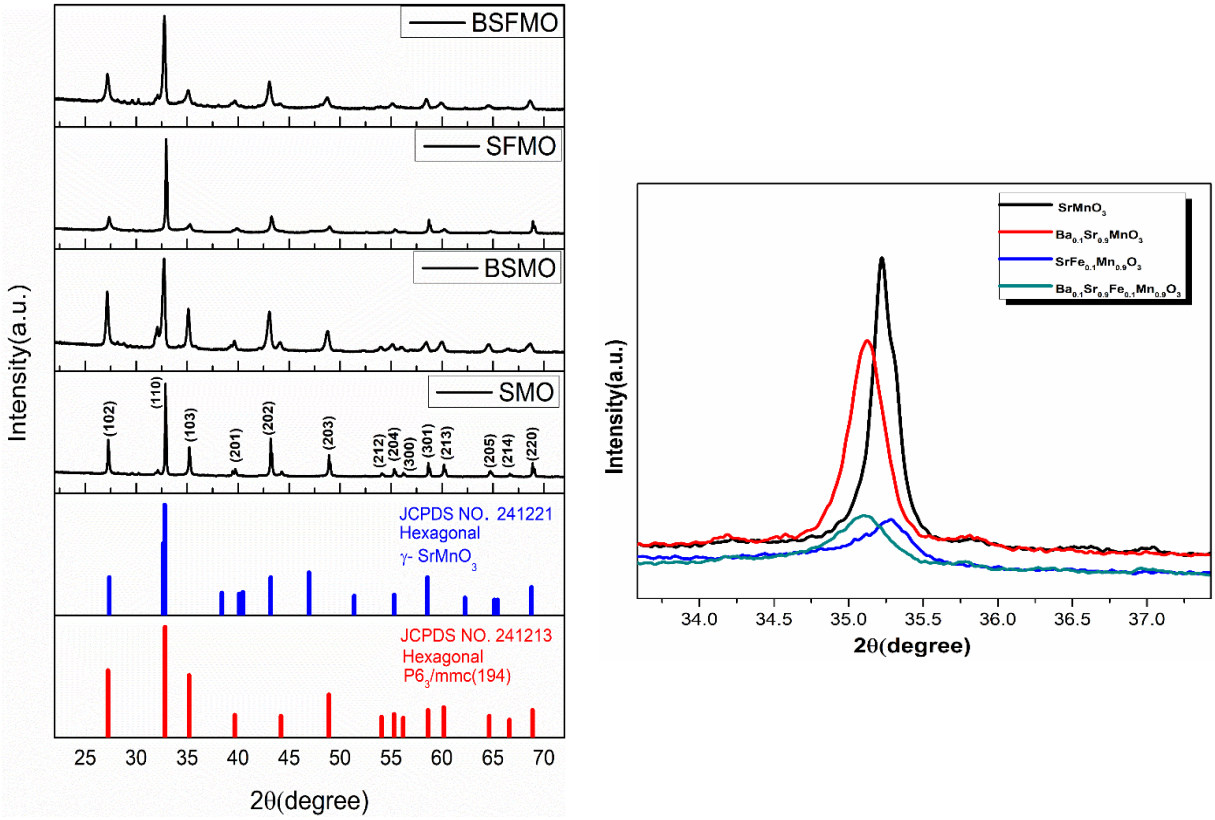

Figure 4.1 – XRD data showing characteristic peaks of (110) with their given JCPDS Card.

X-ray diffraction data is used to calculate the crystallite size using three methods:

1) Debye-Scherrer Formula
2) Williamson-Hall plot

3) Modified Scherrer Formula

1) **Debye-Scherrer Formula :**

$$D = \frac{k\lambda}{\beta cos\theta}$$

where D is Crystallite size, k is Scherrer constant(~ 0.9), λ is X-Ray wavelength(1.5406 Å), β is Full Width at Half Maximum(FWHM) in radians and θ is Bragg's angle in degree.

2) **Williamson-Hall plot:**

$$\beta cos\theta = k\lambda/d + 4\varepsilon sin\theta$$

where graph is plotted between βcosθ and 4sinθ. kλ/d is used to find intercept and ε is give value of microstrain.

3) **Modified Scherrer Formula:**

$$Ln\beta = Ln(k\lambda/d) + Ln(1/cos\theta)$$

where graph is plotted between Lnβ and Ln(1/cosθ) and Ln(kλ/D) is used to calculate intercept.

SrMnO3	Debye-Scherrer Formula	Williamson-Hall Plot	Modified Scherrer Formula
SMO	35.437	86.658	51.1
BSMO	21.819	2.12×10^{-2}	67.547
SFMO	21.886	18.030	22.244
BSFMO	18.970	15.423	35.148

Table 4.1 – Crystallite Sizes with different methods

Crystallite sizes of the synthesized compounds (Table 4.1) were determined using three different analytical methods: Debye-Scherrer Formula, Williamson-Hall Plot and Modified Scherrer Formula resulting in four distinct sets of data. Although the absolute

values obtained from each method varied, a consistent trend was observed: the largest crystallite size was recorded for pure $SrMnO_3$ (SMO), while the smallest was found for the co-doped sample BSFMO (Ba and Fe co-doped $SrMnO_3$) across all methods. This trend aligns well with expectations for a typical doped perovskite system, where doping tends to inhibit grain growth, leading to reduced crystallite size.

4.2.1 Rietveld Refinement

Rietveld refined XRD patterns of pure and doped $SrMnO_3$ are shown in Fig. 4.2, and the estimated lattice parameter and unit cell volume are presented in Table 4.2. The refined weighted-profile factor R_{wp} and profile factor R_p are also indicated in the table. It can be observed the difference in the lattice parameters of the doped $SrMnO_3$ as compared to the pure $SrMnO_3$. This change in the lattice parameters is attributed to the difference in the atomic radii of the dopant ions with respect to the parent ions. In case of BSMO, small amount of secondary phase about 0.44% was detected as $BaMnO_3$.The refined atomic positions of all compounds along with their occupancy are shown in the Tabel 4.3.

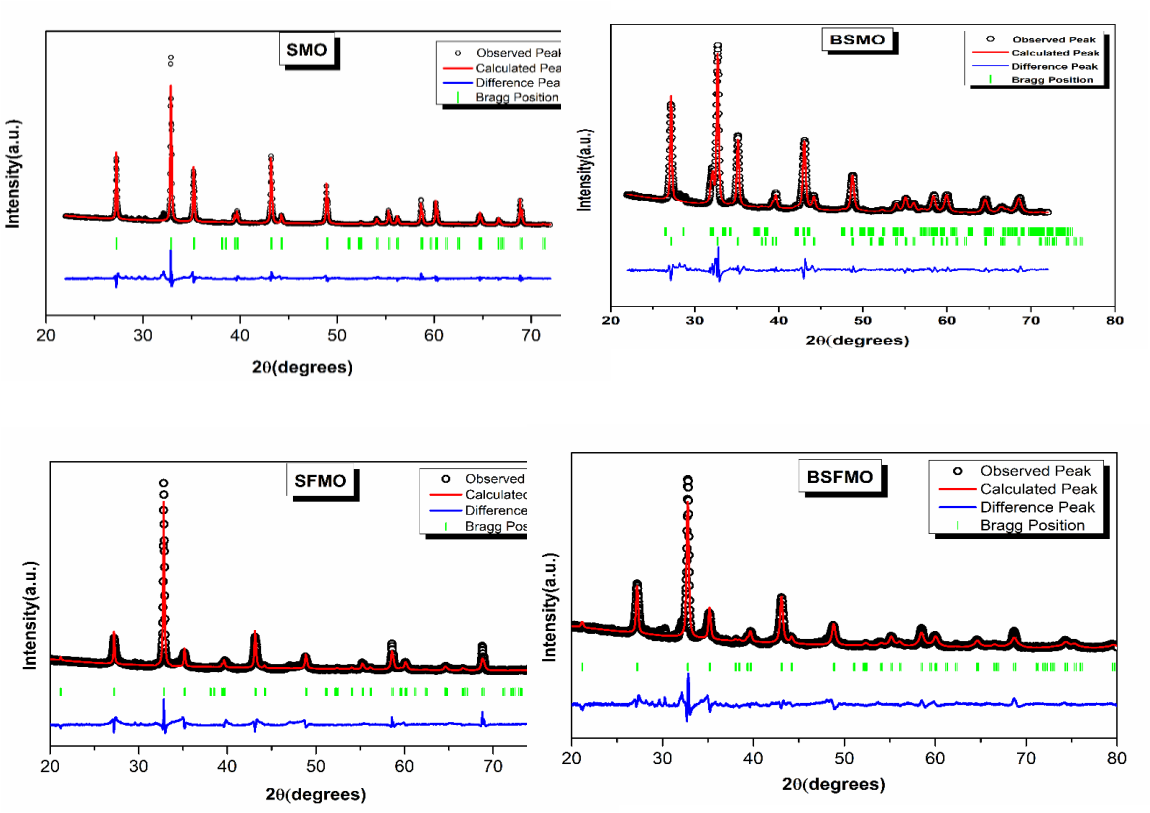

Figure 4.2 – Rietveld Refinement Analysis of $SrMnO_3$ and its Derivatives

Table 4.2 – Structural Parameters of $SrMnO_3$ and its Derivatives

(a)	a (Å)	b (Å)	c (Å)	V $(Å)^3$	χ^2	R_p	R_{wp}
SMO	5.4486	5.4486	9.0793	269.53	10.5	24.7	19.9
BSMO	5.5633	5.5810	9.3559	252.69	8.72	17.3	16.9
SFMO	5.4551	5.4551	9.0913	270.53	14.9	45	34.6
BSFMO	5.4719	5.4719	9.1066	236.14	9.22	29.4	27.4

Table 4.3 – Profile Parameters of $SrMnO_3$ and its Derivatives

(b)	α (°)	β (°)	γ (°)	u	v	w
SMO	90	90	120	-0.034566	0.040626	0.000830
BSMO	90	90	119.556	0.094241	-0.012038	0.012038
SFMO	90	90	120	0.612820	-0.212234	0.194448
BSFMO	90	90	120	2.807056	-1.517029	0.263039

Table 4.4 - Atomic positions of SMO, BSMO, SFMO, BSFMO with occupancy

SMO	x	y	z	Occupancy
Sr1	0.00000	0.00000	0.00000	0.09036
O2	-0.18070	-0.36140	0.25000	0.25720
Sr2	0.33330	0.66670	0.25000	0.08443
Mn1	0.33330	0.66670	0.61289	0.17944
O1	0.50000	0.00000	0.00000	0.37267
BSMO	x	y	z	Occupancy
Sr 1	0.00000	0.00000	0.00000	0.08960
O2	-0.18070	-0.36140	0.25000	0.24027
Sr 2	0.33330	0.66670	0.25000	0.08076

Mn 1	**0.33330**	**0.66670**	**0.61556**	**0.16006**
O1	**0.50000**	**0.00000**	**0.00000**	**0.25833**
Ba1	**0.00000**	**0.00000**	**0.00000**	**-0.00082**
SFMO	**x**	**y**	**z**	**Occupancy**
Sr1	**0.00000**	**0.00000**	**0.00000**	**0.02781**
O2	**-0.13530**	**-0.39383**	**0.25000**	**0.19668**
Sr2	**0.33330**	**0.66670**	**0.25000**	**0.06956**
Mn1	**0.33330**	**0.66670**	**0.61173**	**0.16474**
O1	**0.50000**	**0.00000**	**0.00000**	**0.63476**
Fe1	**0.00000**	**0.00000**	**0.00000**	**0.09714**
BSFMO	**x**	**y**	**z**	**Occupancy**
Sr1	**0.00000**	**0.00000**	**0.00000**	**0.12952**
O2	**-0.18070**	**-0.36140**	**0.25000**	**0.25000**
Sr2	**0.33330**	**0.66670**	**0.25000**	**0.05546**
Mn1	**0.33330**	**0.66670**	**0.61220**	**0.13408**
O1	**0.50000**	**0.00000**	**0.00000**	**0.25000**
Ba1	**0.00000**	**0.00000**	**0.00000**	**-0.23037**
Fe1	**0.00000**	**0.00000**	**0.00000**	**0.41826**

4.3 Raman Analysis

The Raman spectra of pristine $SrMnO_3$ and doped $SrMnO_3$ are studied at room temperature for different samples and shown in figure 4.3. The Raman spectra is used to depict vibrations of different constituent atoms of the compound when it interacts with photons. Raman spectroscopy spans from $300cm^{-1}$ to $900cm^{-1}$. The Raman spectra of $SrMnO_3$ are recorded at room temperature, showing characteristic peaks which match well with standard $SrMnO_3$ structure [44].

The characteristics peaks at 435 cm^{-1} and $639.2cm^{-1}$ refer to the bending and stretching mode of Mn-O vibration. Two more Raman shifts at 548 cm^{-1} and 776 cm^{-1} may corresponds to electron-phonon coupling and Fe-O vibration respectively.

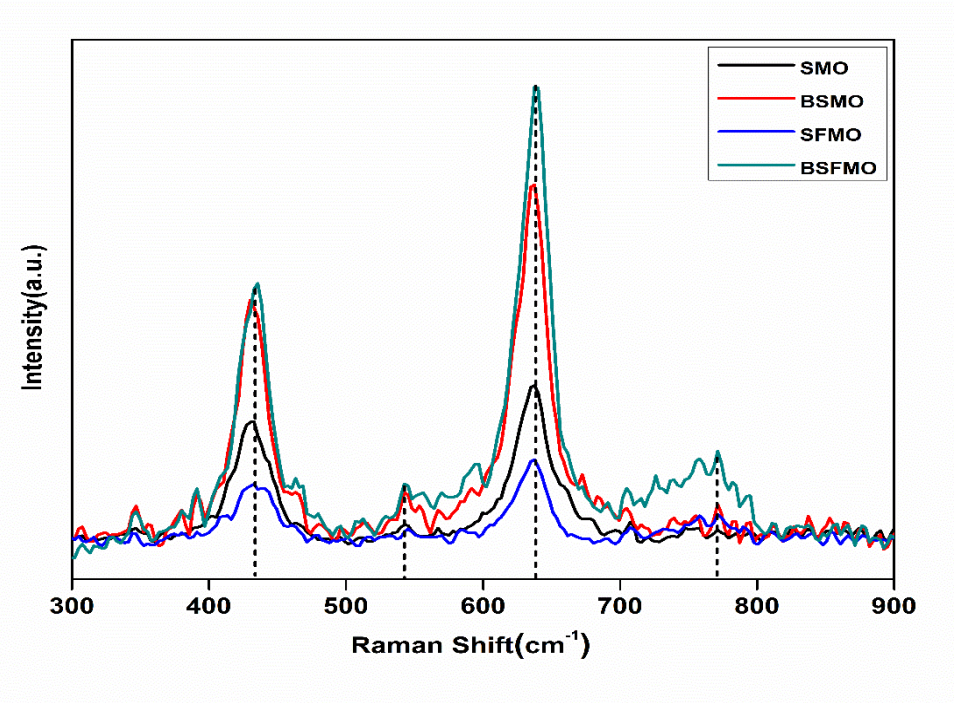

Figure 4.3 – Raman Spectra Analysis of $SrMnO_3$ and its Derivative

4.4 Fourier Transform Infrared Spectroscopy(FTIR)

The FTIR (Fourier Transform Infrared) spectroscopy analysis of $SrMnO_3$, prepared using the sol-gel auto-combustion method, is presented in Fig. 4.4. The peaks at 530.54 cm^{-1} and 607.66 cm^{-1} correspond to the vibrations of the Sr–O bond and the Mn–O stretching vibrations of the MnO_6 octahedron, respectively, which align with findings reported previously[22]. Additionally, the dip at 1462 cm^{-1} is attributed to the asymmetrical broadening of the O–C–O vibration. The sharp peak at 431.19 cm^{-1} can be associated with the A_{1g} and E_{1g} modes, which are characteristic of the Mn_2O_9 moiety. At 1400 cm^{-1}, the trapped nitrates are indicated. The vibrating H_2O group is found between 1400 cm^{-1} and 1650 cm^{-1} [45].

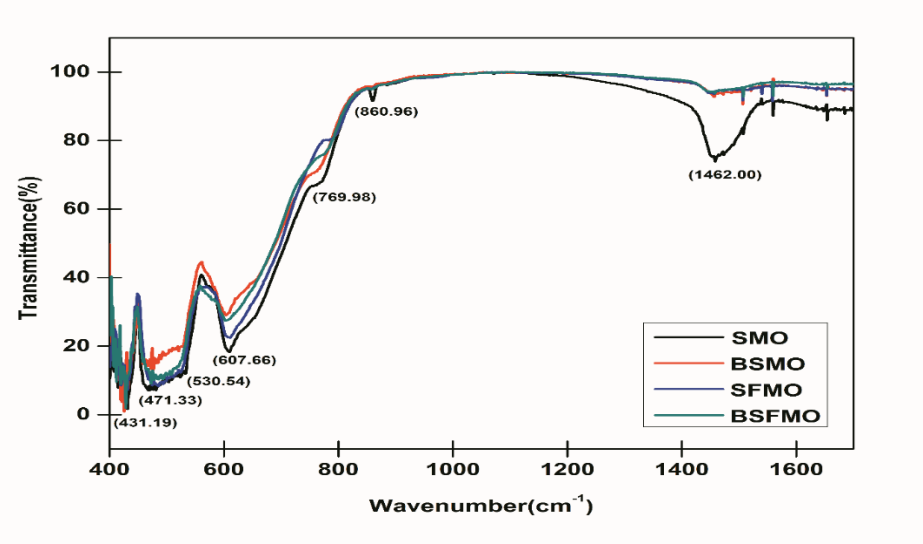

Figure 4.4 – FTIR Spectra analysis

4.5 Dielectric Analysis

Two fundamental properties of dielectric materials are the dielectric constant (ε_r) and the loss tangent (tan δ). The frequency response curves for the dielectric constant and tangent loss are shown in Figures 4.5.

As the frequency increases, the dielectric constant continuously decreases, and found independent towards higher frequency, demonstrating the behavior of a polar dielectric. Out of all synthesized compounds BSFMO shows highest dielectric constant of 523 at 100 Hz, attributed to contributions from electronic, ionic, orientation, and space charge polarizations. The pristine sample SMO has minimum dielectric constant. In terms of loss tangent , there is a similar trend i.e., decreasing trend as frequency increases. This reduction in losses continues at higher temperatures due to the improved characteristics of the high-temperature calcinated sample, as indicated by the quality of the XRD patterns. The minimum loss tangent was observed for BSMO about 0.6 at 100 Hz. Lower losses are generally associated with the development of faster electronic devices[46].

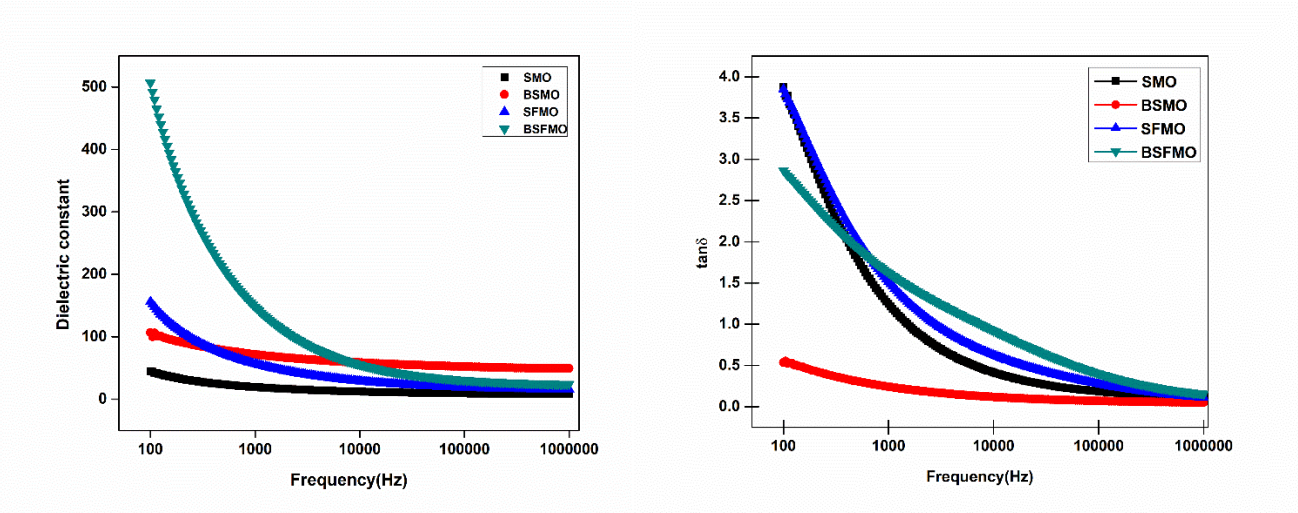

Figure 4.5 – Dielectric constant and tangent loss with changing frequency of SMO, BSMO, SFMO and BSFMO

The plausible explanation regarding dielectric constat variation among all of the compounds i.e., when barium is doped , the dielectric constant and dielectric loss fall, possibly due to impurities and charge defects in the samples[47]. Due to doping, incorporation of Ba^{2+} affects structural deformation but with minimal impact on dielectric constant. At a specific frequency known as the relaxation frequency, the dielectric constant exhibits saturation behavior. The reduction in the dielectric constant and the presence of a high relaxation frequency can be attributed to the Maxwell-Wagner effect[48]. According to Maxwell-Wagner theory, polarization occurs among charged particles at the interfaces between grains and pores, a phenomenon referred to as interfacial polarization. As the frequency changes, the polarity at these grain and pore interfaces also changes. As the frequency increases, this polarity shifts rapidly, and eventually, at sufficiently high frequencies, the charges do not have enough time to adjust their positions. This leads to the occurrence of the relaxation phenomenon[48].

Doping iron at B-site increases the value of ε_r at low frequencies due to interfacial and space charge polarization from its inhomogeneous dielectric structure. As frequency rises, polarization decreases and stabilizes because multiple defects create inhomogeneous dipoles that can't follow the external electric field's frequency. This enhances the space charge effect on polarization, and doping further reduces interfacial polarization caused by these existing defects[49].

The dielectric loss, represents the energy dissipation in the dielectric system. The loss tangent decreases continuously with increasing frequency. The dispersion in tan δ is seen in the lower frequency region. Due to Fe^{3+} incorporation with Mn^{2+}, electron hopping happens which leads to strong electron phonon interaction and shows increased energy dissipation as we see in Figure 4.5[49].

4.6 Polarization-Electric Field Loop Analysis

Fig. 4.6 shows PE hysteresis loop of SMO and its doped derivative. The loop of $SrMnO_3$ is in bulky oval shape. This is due to higher leakage current. The Remanent polarization decreases from 0.774 μC/cm^2 to 0.331 μC/cm^2 as we doped Ba at A-site but increases when Fe is doped at B- site(0.447 μC/cm^2). The value of P_r is larger for Co-doped sample but still lower than pristine sample(0.675 μC/cm^2) but coercive field is almost equal for all samples.

It is observed that when Ba is doped in A-site of this single perovskite structure, its curve shrinks and its value of remanent polarization decreases. This is due to the incorporation of Ba^{2+} in Sr^{2+} which leads to the volume expansion and possibly shows weaker ferroelectric ordering[50]. When Fe is doped , the remnant polarization increases due to incorporation of Fe^{3+} with Mn^{2+} showing mixed valence state leads to structural distortion and possibly decreases its antiferroelectric behaviour and ferroelectric behaviour strengthens[50]. When SMO is codoped at a and B site simultaneously, we observe the combined effect of both doping and it strengthen the ferroelectric behaviour.

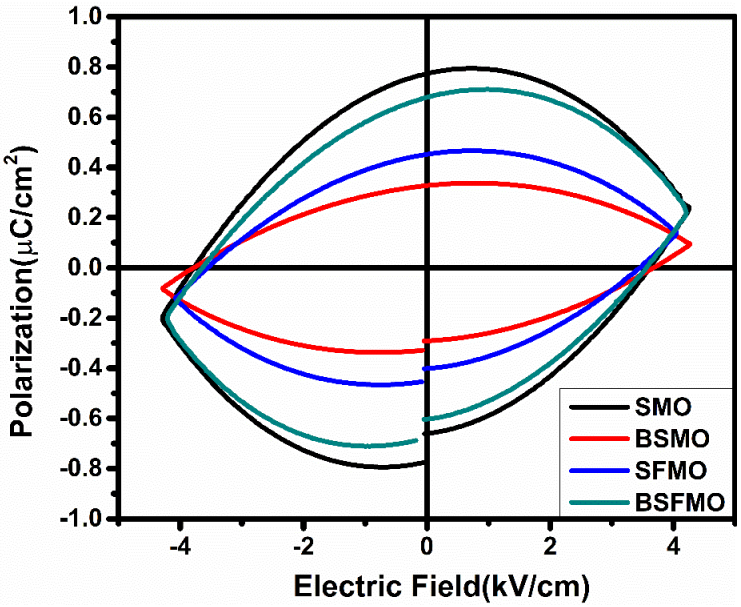

Figure 4.7 – Combined P-E Loop of all samples

4.7 Magnetic Properties

$SrMnO_3$ is known for its G type antiferromagnetic nature showing transition temperature at 280K from antiferromagnetic behaviour to paramagnetic behaviour[51]. The analysis of magnetic properties has been done by the MPMS3 SQUID magnetometer at the magnetic field at maximum ±18000 Oe. The analysis is done at the room temperature(300K).

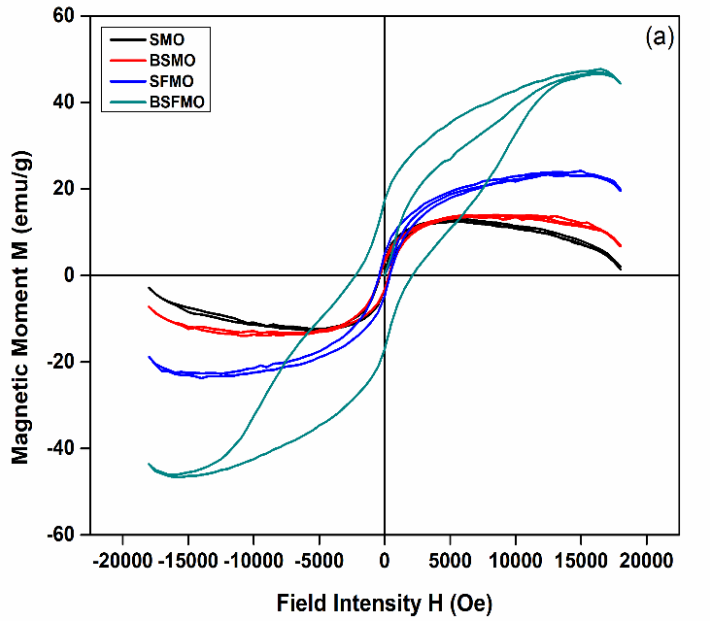

Figure 4.8 – (a) M-H hysteresis curve

Fig. 4.7 shows the hysteresis curve of SMO and its derivatives. As we can see that SMO shows antiferromagnetic behaviour as curve is narrow. As we doped Ba in the A-site, it starts changing its behaviour from antiferromagnetic to ferromagnetic behaviour. Similar thing happens when Fe is doped at B site. When doped simultaneously at both sites, it shows hysteresis curve at room temperature, showing ferromagnetic behaviour.

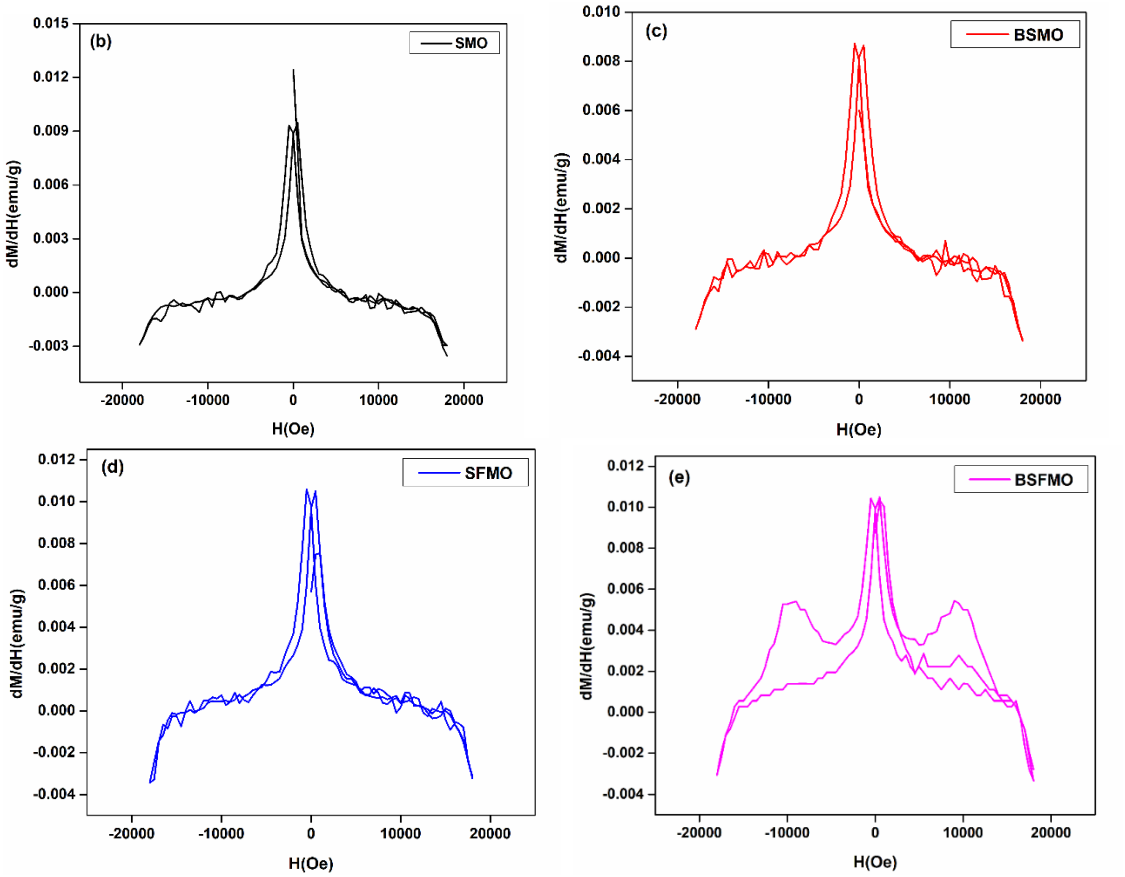

Figure 4.9 – dM/dH curve of (b) SMO, (c) BSMO, (d) SFMO, (e)BSFMO

Table 4.5 – Remanent Polarization and Coercive Field value of SMO and its Doped Derivative.

	SMO	BSMO	SFMO	BSFMO
Remnant Magnetization(emu/g)	**0.02174**	**0.02166**	**0.03015**	**0.10458**
Coercive field(Oe)	**343.6826**	**368.9295**	**418.4328**	**2219.7699**

Barium-doped $SrMnO_3$ samples exhibit significantly weak ferromagnetism. This is demonstrated by the transition of the magnetization (M) versus magnetic field (H) loops from an antiferromagnetic curve to a weak ferromagnetic curve as a result of barium doping. The emergence of ferromagnetic ordering can be attributed to the double exchange interactions between Mn^{2+} and Mn^{3+} ions facilitated by O^{2-} oxygen ions[52]. Similarly, Fe – doped $SrMnO_3$ exhibit weak ferromagnetism due to mixed valence state of Mn^{2+} and Fe^{3+}[53]. When we doped Ba and Sr simultaneously then it shows combined effect of Co-doping which leads to better M-H curve and which indicated ferromagnetic behaviour. The observed double hysteresis loop in the magnetization curve of BSFMO indicates the presence of two competing magnetic exchange pathways: Fe–O–Fe and Fe–O–Mn. The Fe–O–Fe interaction is typically associated with antiferromagnetic or weak ferromagnetic coupling, while the Fe–O–Mn interaction often promotes stronger ferromagnetic alignment due to superexchange mechanisms. The coexistence and mutual interference of these two interactions lead to a complex magnetic ground state, which is reflected in the form of a composite double hysteresis loop. This behavior suggests magnetic phase separation or exchange bias-like effects, arising from the interplay between different local magnetic environments within the lattice.

Figure 4.8 represent the differential susceptibility (dM/dH) as a function of magnetic field (H), which highlights the rate of change of magnetization. The distinct double-peak feature in BSFMO strongly supports the presence of competing magnetic interactions. This complex interplay could be key to realizing exchange bias, magnetoresistance.

CHAPTER 5

CONCLUSION AND FUTURE SCOPE

5.1 Conclusions

The pure perovskite phase of $SrMnO_3$ (SMO) and its doped derivatives i.e. Ba-substituted (BSMO), Fe-substituted (SFMO), and Ba + Fe co-substituted (BSFMO) were successfully synthesized via the sol-gel auto-combustion method. The structural evolution of these compounds was comprehensively examined using Rietveld refinement of X-ray diffraction data, confirming the formation of the intended perovskite phase in all samples. Notably, no secondary phases were detected in SMO, SFMO, and BSFMO. However, a minor secondary phase of $BaMnO_3$, amounting to approximately 0.44 wt%, was identified in the BSMO sample, suggesting slight phase segregation upon Ba doping at the A-site.

The local vibrational dynamics of the lattice were investigated through FTIR and Raman spectroscopy, which revealed systematic shifts and weakening of the Sr–O and Mn–O stretching modes upon doping. These observations affirm the influence of both A-site (Ba) and B-site (Fe) substitutions on the lattice symmetry and bond strength, indicating enhanced structural distortion or reduced bonding stiffness.

Dielectric measurements showed that the co-doped BSFMO sample exhibited enhanced dielectric properties, including a higher dielectric constant and lower loss tangent compared to the singly doped or undoped samples. This improvement can be attributed to the synergistic effect of A-site and B-site dopants, which likely promote charge carrier localization and interfacial polarization.

Magnetically, the BSFMO compound displayed an unusual double hysteresis loop in its magnetization measurements, which is indicative of coexisting and competing magnetic interactions. This behavior suggests the presence of both Fe–O–Fe and Fe–O–Mn exchange interactions, giving rise to a complex magnetic ground state. The interaction and interference between these magnetic sublattices are believed to be responsible for the observed double-loop feature, supporting the scenario of magnetic phase coexistence or spin frustration in the co-doped system.

5.2 Future Scope

This work holds significant potential within the current landscape of electronic materials research. With further investigation, particularly into spin polarization, carrier transport mechanisms, and interfacial magnetic coupling these materials could pave the way toward establishing themselves as promising candidates for spintronic device applications.

- ✓ Temperature dependent ferromagnetic properties need to be investigated in order to clarify the possible magnetic transitions.
- ✓ To further strengthen its magnetic properties such as presence of double hysteresis loop may be supported by XPS.
- ✓ Thin film deposition may influence the ferroelectric ordering and thus improves its PE loop.
- ✓ Magnetoresistance measurement would be significantly proving the candidature of its potential regarding its functional properties.

References

[1] Spaldin, Nicola A., and Manfred Fiebig. "The renaissance of magnetoelectric multiferroics." *Science* 309.5733 (2005): 391-392.

[2] A. J. C. Buurma, G. R. Blake, T. T. M. Palstra, and U. Adem, "Multiferroic Materials: Physics and Properties," in *Reference Module in Materials Science and Materials Engineering*, Elsevier, 2016. doi: 10.1016/b978-0-12-803581-8.09245-6.

[3] N. A. Spaldin, "Multiferroics: Past, present, and future," May 01, 2017, *Cambridge University Press*. doi: 10.1557/mrs.2017.86.

[4] M. Fiebig, T. Lottermoser, D. Meier, and M. Trassin, "The evolution of multiferroics," Jul. 05, 2016, *Nature Publishing Group*. doi: 10.1038/natrevmats.2016.46.

[5] D. Khomskii, "Classifying multiferroics: Mechanisms and effects," *Physics (College Park Md)*, vol. 2, Mar. 2009, doi: 10.1103/physics.2.20.

[6] Junling. Wang, *Multiferroic materials : properties, techniques, and applications*. CRC Press, 2017.

[7] G. Liu, S. Zhang, W. Jiang, and W. Cao, "Losses in ferroelectric materials," 2015, *Elsevier Ltd*. doi: 10.1016/j.mser.2015.01.002.

[8] P. Rasaili, N. K. Sharma, and A. Bhattarai, "Comparison of Ferromagnetic Materials: Past Work, Recent Trends, and Applications," Mar. 01, 2022, *MDPI*. doi: 10.3390/condmat7010012.

[9] Zener, C., and R. R. Heikes. "Exchange interactions." *Reviews of Modern Physics* 25.1 (1953): 191.

[10] J. A. Alonso, "Electronic and Atomic Structure, and Magnetism of Transition-Metal Clusters," 2000, *American Chemical Society*. doi: 10.1021/cr980391o.

[11] Tilley, Richard JD. *Perovskites: structure-property relationships*. John Wiley & Sons, 2016.

[12] A. S. Bhalla, R. Guo, and R. Roy, “The perovskite structure - A review of its role in ceramic science and technology,” 2000, *Springer New York*. doi: 10.1007/s100190000062.

[13] P. G. R. Achary, A. A. Nayak, R. K. Bhuyan, R. N. P. Choudhary, and S. K. Parida, “Effect of cerium dopant on the structural and electrical properties of SrMnO3 single perovskite,” *J Mol Struct*, vol. 1226, Feb. 2021, doi: 10.1016/j.molstruc.2020.129391.

[14] F. Wang *et al.*, “Oxygen vacancy formation, crystal structures, and magnetic properties of three SrMnO3-δ films,” *Appl Phys Lett*, vol. 109, no. 5, Aug. 2016, doi: 10.1063/1.4960463.

[15] Cheong, Sang-Wook, and Maxim Mostovoy. "Multiferroics: a magnetic twist for ferroelectricity." *Nature materials* 6.1 (2007): 13-20.

[16] S. Demirel *et al.*, “Structural, magnetic, electrical and electrochemical properties of SrCoO2.5, Sr9Co2Mn5O21 and SrMnO3 compounds,” *Ceram Int*, vol. 43, no. 17, pp. 14818–14826, Dec. 2017, doi: 10.1016/j.ceramint.2017.07.230.

[17] C. Doroftei, P. D. Popa, E. Rezlescu, and N. Rezlescu, “Nanocrystalline SrMnO3 powder as catalyst for hydrocarbon combustion,” *J Alloys Compd*, vol. 584, pp. 195–198, 2014, doi: 10.1016/j.jallcom.2013.09.054.

[18] P. Aich *et al.*, “Fluorinated hexagonal 4H SrMnO3: a locally disordered manganite,” *J Mater Chem C Mater*, vol. 7, no. 12, pp. 3560–3568, 2019, doi: 10.1039/c8tc04293d.

[19] G. George *et al.*, “Effect of doping on the performance of high-crystalline SrMnO3 perovskite nanofibers as a supercapacitor electrode,” *Ceram Int*, vol. 44, no. 17, pp. 21982–21992, Dec. 2018, doi: 10.1016/j.ceramint.2018.08.313.

[20] S. Hashimoto and H. Iwahara, “Structural, Thermal and Electrical Properties of Ce-Doped SrMnO 3,” 2000.

[21] M. Khazaei, A. Malekzadeh, F. Amini, Y. Mortazavi, and A. Khodadadi, "Effect of citric acid concentration as emulsifier on perovskite phase formation of nano-sized SrMnO3 and SrCoO3 samples," *Crystal Research and Technology*, vol. 45, no. 10, pp. 1064–1068, Oct. 2010, doi: 10.1002/crat.201000258.

[22] A. Saleem *et al.*, "Structural, electronic and optical properties of SrMnO3 photocatalyst for dye degradation: Experimental and DFT study," *J Alloys Compd*, vol. 1010, Jan. 2025, doi: 10.1016/j.jallcom.2024.176922.

[23] C. J. Yoon *et al.*, "Defect induced polar distortion in SrMnO3 thin films," *Appl Surf Sci*, vol. 683, Feb. 2025, doi: 10.1016/j.apsusc.2024.161802.

[24] A. Sutka and G. Mezinskis, "Sol-gel auto-combustion synthesis of spinel-type ferrite nanomaterials," Jun. 2012. doi: 10.1007/s11706-012-0167-3.

[25] Niederberger, Markus, and Nicola Pinna. *Metal oxide nanoparticles in organic solvents: synthesis, formation, assembly and application*. Springer Science & Business Media, 2009.

[26] S. L. González-Cortés and F. E. Imbert, "Fundamentals, properties and applications of solid catalysts prepared by solution combustion synthesis (SCS)," Feb. 15, 2013. doi: 10.1016/j.apcata.2012.11.024.

[27] E. Carlos, R. Martins, E. Fortunato, and R. Branquinho, "Solution Combustion Synthesis: Towards a Sustainable Approach for Metal Oxides," Jul. 27, 2020, *Wiley-VCH Verlag*. doi: 10.1002/chem.202000678.

[28] A. Eivazihollagh, I. Svanedal, H. Edlund, and M. Norgren, "On chelating surfactants: Molecular perspectives and application prospects," Mar. 15, 2019, *Elsevier B.V.* doi: 10.1016/j.molliq.2019.01.076.

[29] A. C. F. M. Costa, A. M. D. Leite, H. S. Ferreira, R. H. G. A. Kiminami, S. Cava, and L. Gama, "Brown pigment of the nanopowder spinel ferrite prepared by combustion reaction," *J Eur Ceram Soc*, vol. 28, no. 10, pp. 2033–2037, 2008, doi: 10.1016/j.jeurceramsoc.2007.12.039.

[30] Costa, A. C. F. M., et al. "Brown pigment of the nanopowder spinel ferrite prepared by combustion reaction." *Journal of the European Ceramic Society* 28.10 (2008): 2033-2037.

[31] L. Yu, S. Cao, Y. Liu, J. Wang, C. Jing, and J. Zhang, “Thermal and structural analysis on the nanocrystalline NiCuZn ferrite synthesis in different atmospheres,” *J Magn Magn Mater*, vol. 301, no. 1, pp. 100–106, Jun. 2006, doi: 10.1016/j.jmmm.2005.06.020.

[32] K. H. Wu, C. H. Yu, Y. C. Chang, and D. N. Horng, “Effect of pH on the formation and combustion process of sol-gel auto-combustion derived NiZn ferrite/SiO 2 composites,” *J Solid State Chem*, vol. 177, no. 11, pp. 4119–4125, Nov. 2004, doi: 10.1016/j.jssc.2004.07.056.

[33] Y. Waseda, E. Matsubara, and K. Shinoda, “X-Ray Diffraction Crystallography X-Ray Diffraction Crystallography Introduction, Examples and Solved Problems.”

[34] A. Pandey, S. Dalal, S. Dutta, and A. Dixit, “Structural characterization of polycrystalline thin films by X-ray diffraction techniques,” Jan. 01, 2021, *Springer*. doi: 10.1007/s10854-020-04998-w.

[35] A. Kudelski, “Analytical applications of Raman spectroscopy,” Jun. 30, 2008, *Elsevier*. doi: 10.1016/j.talanta.2008.02.042.

[36] Larkin, Peter. *Infrared and Raman spectroscopy: principles and spectral interpretation*. Elsevier, 2017.

[37] G. S. Bumbrah and R. M. Sharma, “Raman spectroscopy – Basic principle, instrumentation and selected applications for the characterization of drugs of abuse,” Sep. 01, 2016, *Egyptian Forensic Medicine Authority*. doi: 10.1016/j.ejfs.2015.06.001.

[38] C. Berthomieu and R. Hienerwadel, “Fourier transform infrared (FTIR) spectroscopy,” Sep. 2009. doi: 10.1007/s11120-009-9439-x.

[39] Griffiths, Peter R. "Fourier transform infrared spectrometry." *Science* 222.4621 (1983): 297-302.

[40] A. Shahee, N. P. Lalla, and T. Shripathi, “A simple and low cost Sawyer-Tower ferro-electric loop tracer with variable frequency and compensation circuit,” 2009. [Online]. Available: https://www.researchgate.net/publication/225038617

[41] M. S. Venkatesh and G. S. V Raghavan, “An overview of dielectric properties measuring techniques,” 2005.

[42] R. C. Black and F. C. Wellstood, “Measurements of Magnetism and Magnetic Properties of Matter,” in *The SQUID Handbook: Applications of SQUIDs and SQUID Systems*, vol. 2, John Wiley and Sons, 2006, pp. 391–440. doi: 10.1002/9783527609956.ch12.

[43] E Sinn, University of Hull, Hull, UK & 2005, Elsevier Ltd.

[44] A. Sacchetti, M. Baldini, P. Postorino, C. Martin, and A. Maignan, “Raman spectroscopy on cubic and hexagonal SrMnO3,” *Journal of Raman Spectroscopy*, vol. 37, no. 5, pp. 591–596, 2006, doi: 10.1002/jrs.1484.

[45] R. R. Awasthi and B. Das, “Structural transition and tunable optical, morphological and magnetic properties of Mn-doped BiFeO3 films,” *Optik (Stuttg)*, vol. 194, Oct. 2019, doi: 10.1016/j.ijleo.2019.162973.

[46] Barsoum, Michel. *Fundamentals of ceramics*. CRC press, 2019.

[47] G. M. Sravani *et al.*, “Synthesis, structural, improved magnetic and electrical properties of Sr2+ doped BiFeO3 multiferroic materials,” *Appl Phys A Mater Sci Process*, vol. 130, no. 11, Nov. 2024, doi: 10.1007/s00339-024-07972-z.

[48] M. Asif Iqbal, M. U. Islam, I. Ali, M. A. Khan, I. Sadiq, and I. Ali, “High frequency dielectric properties of Eu+3-substituted Li-Mg ferrites synthesized by sol-gel auto-combustion method,” *J Alloys Compd*, vol. 586, pp. 404–410, 2014, doi: 10.1016/j.jallcom.2013.10.066.

[49] E. Hastuti, A. Subhan, P. Amonpattaratkit, M. Zainuri, and S. Suasmoro, “The effects of Fe-doping on MnO2: phase transitions, defect structures and

its influence on electrical properties," *RSC Adv*, vol. 11, no. 14, pp. 7808–7823, Jan. 2021, doi: 10.1039/d0ra10376d.

[50] R. He, I. Hong, S. Kim, and C. W. Bark, "Review on recent developments in the ferroelectric material SrMnO3," Sep. 01, 2025, *Elsevier B.V.* doi: 10.1016/j.hybadv.2025.100456.

[51] H. Wang, G. Lu, W. Tan, and H. Wang, "The structure, magnetic properties, magnetotransport and temperature coefficient of resistivity of hexagonal 4H-SrMnO3 manganite," *J Alloys Compd*, vol. 1008, Dec. 2024, doi: 10.1016/j.jallcom.2024.176718.

[52] C. Qian *et al.*, "Effects of Ba doping on the structural, magnetic and microwave absorption properties for LaMnO3 perovskites," *Journal of Materials Science: Materials in Electronics*, vol. 35, no. 20, Jul. 2024, doi: 10.1007/s10854-024-13162-7.

[53] D. D. Dung, N. T. Hung, and D. Odkhuu, "Structure, optical and magnetic properties of new Bi0.5Na0.5TiO3- SrMnO3−δ solid solution materials," *Sci Rep*, vol. 9, no. 1, Dec. 2019, doi: 10.1038/s41598-019-54172-4.